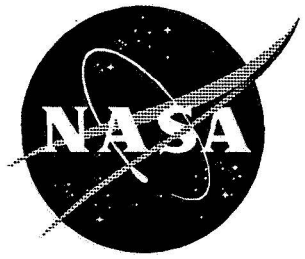

NASA Contractor Report 4721

GPS Attitude Determination Using Deployable-Mounted Antennas

Michael L. Osborne and Robert H. Tolson

Cooperative Agreement NCC1-104
Prepared for Langley Research Center

March 1996

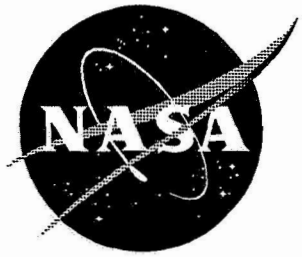

NASA Contractor Report 4721

GPS Attitude Determination Using Deployable-Mounted Antennas

Michael L. Osborne and Robert H. Tolson
The George Washington University
Joint Institute for Advancement of Flight Sciences
Langley Research Center • Hampton, Virginia

National Aeronautics and Space Administration
Langley Research Center • Hampton, Virginia 23681-0001

Prepared for Langley Research Center
under Cooperative Agreement NCC1-104

March 1996

Printed copies available from the following:

NASA Center for AeroSpace Information
800 Elkridge Landing Road
Linthicum Heights, MD 21090-2934
(301) 621-0390

National Technical Information Service (NTIS)
5285 Port Royal Road
Springfield, VA 22161-2171
(703) 487-4650

Abstract

The primary objective of this investigation is to develop a method to solve for spacecraft attitude in the presence of potential incomplete antenna deployment. Most research on the use of the Global Positioning System (GPS) in attitude determination has assumed that the antenna baselines are known to less than 5 centimeters, or one quarter of the GPS signal wavelength. However, if the GPS antennas are mounted on a deployable fixture such as a solar panel, the actual antenna positions will not necessarily be within 5 cm of nominal. Incomplete antenna deployment could cause the baselines to be grossly in error, perhaps by as much as a meter. Overcoming this large uncertainty in order to accurately determine attitude is the focus of this study. To this end, a two-step solution method is proposed. The first step uses a least-squares estimate of the baselines to geometrically calculate the deployment angle errors of the solar panels. For the spacecraft under investigation, the first step determines the baselines to 3-4 cm with 4-8 minutes of data. A Kalman filter is then used to complete the attitude determination process, resulting in typical attitude errors of 0.5°.

Table of Contents

Nomenclature

$\hat{}$	estimate
$\| \ \|$	norm
$\mathbf{b}$	baseline vector
${}^{B}\mathbf{C}^{I}$	inertial to body transformation matrix
E[ ]	Expectation value
$\tilde{\mathbf{e}}_j$	unit vector to j^{th} GPS SV
$e(t_k)$	prediction error at time t_k
$G^{-1}[m,n]$	shaping filter of order [m,n]
$\mathbf{H}$	observation matrix
$\mathbf{K}$	Kalman filter gain matrix
K	integer-line bias parameter
k	differential phase integer count
$\mathbf{P}$	state covariance matrix
$\mathbf{Q}$	state noise covariance matrix
q^{-1}	delay operator
$\mathbf{R}$	measurement noise covariance matrix
$\mathbf{r}$	position vector of GPS antenna in inertial reference frame
$\mathbf{r}_j$	position vector of j^{th} SV in inertial reference frame
$y(t_k)$	simulated differential phase residual at time t_k
$z(t_k)$	measured differential phase residual at time t_k

Φ	state transition matrix
ΔR	differential range
$\Delta\varphi$	differential phase
α	flap angle
β	line bias
λ	L1 GPS carrier wavelength
μ	differential phase measurement noise

List of Abbreviations

ACS	Attitude Control System
ARMA	Auto-Regressive Moving-Average
BCS	Body Coordinate System
DAE	Deployment Angle Error
ECEF	Earth-Centered Earth-Fixed
ECI	Earth-Centered Inertial
GPS	Global Positioning System
JSC	Johnson Space Center
PRN	Pseudo-Random Number
PSD	Power Spectral Density
RMS	Root Mean Square
SV	Space Vehicle
TRACE	Transition Region and Coronal Explorer

List of Figures

List of Tables

1. Introduction

Attitude determination by means of GPS measurements is a continually evolving field. Early studies indicated that GPS is a feasible alternative to more expensive inertial guidance instruments aboard low orbiting spacecraft[1]. Aircraft test flights soon validated this by showing that real-time attitude information could be obtained from GPS measurements[2].

Attitude determination utilizing GPS amounts to calculating the baseline vector from one GPS antenna to another. Errors in this vector directly affect the accuracy to which attitude can be found. One of the early simulations suggested that attitude accuracies of 0.3° would be possible using antenna baselines of 1 meter[3]. Ground-based experiments later showed that a 1.78 m baseline vector can be determined within 1-3 cm[4]. This uncertainty in the baseline translates into an attitude error closer to 1°.

In the previously mentioned studies, the baselines vectors were assumed to be known in a body reference frame. As the study of GPS-based attitude determination became more involved, the problem of correctly locating the baselines in the body frame of a spacecraft came under scrutiny. Errors in the position of the GPS antennas in the body frame add to the total attitude error. One investigation into this problem involved the RADCAL satellite and concentrated on the effects of 5-10 cm errors in the positions of the antennas[5]. In that study, a succession of estimates was used to decrease first attitude and then baseline uncertainties beginning with some baseline assumptions. In this investigation, the baselines are not known well enough for an initial attitude determination. Consequently, another approach must be taken.

The Transition-Region and Coronal Explorer, or TRACE, spacecraft presents a unique problem in the study of GPS attitude determination. TRACE is slated to join the growing number of earth-orbiting observatories developed by NASA in recent years. The science mission of TRACE involves extended study of the sun, including time-elapsed filming of solar activity. In addition to the standard compliment of magnetometers and gyroscopes for the attitude control system, the spacecraft will also be equipped with a GPS receiver to study the usefulness of space-borne GPS attitude determination. The unique property of TRACE is that the GPS antennas are to be mounted on three deployable solar panels. The possibility exists that the panels may fail to fully deploy, causing the positions of the antennas to deviate from their intended nominal values. Thus the baselines are not known well enough to obtain accurate attitude knowledge in the body frame. To solve this problem, the nominal attitude of the spacecraft is used to solve for the baselines in inertial space, and the deployment angle errors of the solar panels are estimated geometrically. A Kalman filter is then used to determine the TRACE attitude continuously.

To familiarize the reader with GPS-based attitude determination, the governing equations will first be presented. This is succeeded by a discussion of a noise model, which was developed from ground-test data to add realism to the simulations. The TRACE spacecraft is then examined, and a method to determine its attitude is proposed. This is followed by the results of this method for TRACE and some concluding remarks.

2. Governing Equations

The basic equations governing the use of GPS for attitude determination are introduced in this section. The first to be presented are the geometric equations for attitude determination. This is followed by a discussion of Kalman filters, which will be used to sequentially process GPS measurements for attitude information.

2.1 Attitude Determination Using Differential Phase

Determining attitude by any method is equivalent to finding the orientation of one coordinate system with respect to another. The relationship between two coordinate systems, which define two frames of reference, may be expressed by a transformation matrix. The use of the transformation matrix allows one to convert the components of a vector in one frame to the appropriate components in the other frame. The goal of attitude determination, then, is to determine the transformation matrix between the spacecraft body frame and some inertial frame.

2.1.1 Body Frame Definition

A coordinate system is fully described by the position of the origin, the fundamental plane, the principal direction within the plane, and the sense of the normal to the plane[6]. In attitude determination, however, only the orientation of one frame with respect to another is of importance: the origin of the system may be disregarded. One unit vector is chosen to point in the fundamental direction of the coordinate system and another is chosen to point in the direction of the outward normal to the plane; the third vector is chosen to complete a right-handed orthonormal triad.

In GPS-based attitude determination, the vector from one GPS antenna to another defines a baseline in the Earth-Centered Inertial, or ECI, reference frame. Now, since any two nonparallel vectors form a plane, the attitude of a spacecraft can be fully determined by two such vectors. As a result, a set of three GPS antennas forming two nonparallel baselines is sufficient to determine attitude. What is sought is the transformation matrix between the inertial reference frame in which the baselines are found from GPS measurements and a body reference frame in which these vectors are fixed. The following provides a method for finding this matrix.

Two baselines $\mathbf{b}_1$ and $\mathbf{b}_2$ may be used to define a body reference frame by using the set of equations

$$\tilde{\mathbf{i}}^B = \frac{\mathbf{b}_1}{\|\mathbf{b}_1\|}, \quad \tilde{\mathbf{k}}^B = \frac{\mathbf{b}_1 \times \mathbf{b}_2}{\|\mathbf{b}_1 \times \mathbf{b}_2\|}, \quad \tilde{\mathbf{j}}^B = \tilde{\mathbf{k}}^B \times \tilde{\mathbf{i}}^B. \tag{1}$$

The plane of the two baselines forms the fundamental plane, and the first baseline vector $\mathbf{b}_1$ is normalized to form the fundamental direction $\tilde{\mathbf{i}}^B$ of the body frame. The normal to the plane $\tilde{\mathbf{k}}^B$ is formed by normalizing the cross product of the two baselines. The third unit vector completes the triad, which is then used to form the transformation matrix from the inertial frame to the body frame:

$${}^B\mathbf{C}^I = \begin{bmatrix} \left(\tilde{\mathbf{i}}^B\right)^{\mathrm{T}} \\ \left(\tilde{\mathbf{j}}^B\right)^{\mathrm{T}} \\ \left(\tilde{\mathbf{k}}^B\right)^{\mathrm{T}} \end{bmatrix}. \tag{2}$$

An Euler angle representation of the attitude can be extracted from this matrix for a more intuitive understanding of the orientation of the spacecraft in inertial space.

2.1.2 Differential Phase Equations

The signals broadcast by the GPS space vehicles, or SV's, are carried on electromagnetic waves of two frequencies: L1 (1575.42 MHz) and L2 (1227.6 MHz)[7]. Although the contents of the signals allow one to determine the position of a GPS antenna and the SV's, the carrier waves themselves are employed in GPS attitude determination.

The primary observable in GPS attitude determination is differential phase. This quantity will be described with the aid of Figure 1. In this figure, a vector from Antenna 1 to Antenna 2 defines a baseline **b** in the inertial frame. A GPS SV is located in the direction of the unit vector $\tilde{\mathbf{e}}_j$. The satellite position in ECI coordinates, $\mathbf{r}_j$, is calculated from the ephemerides which are broadcast as part of the GPS signal[8]. The signal can also provide the positions of the two antennas to about 30 meters by using the methods for GPS position determination discussed in many texts[9]. Assuming the baseline is only a few meters or less in length, the two antenna positions will be nearly the same in ECI coordinates and may both be represented by **r**. The unit vector to the j^{th} SV can then be found from

$$\tilde{\mathbf{e}}_j = \frac{\mathbf{r}_j - \mathbf{r}}{\left\| \mathbf{r}_j - \mathbf{r} \right\|}. \qquad (3)$$

The wave sent to the antennas from the SV propagates in the direction indicated in the figure. Antenna 2 is the first to receive the signal because it is closer to the SV than Antenna 1 by an amount ΔR. This range difference is the projection of the baseline onto the unit vector to the SV. Thus ΔR is computed by taking the dot product of **b** and $\tilde{\mathbf{e}}$ and

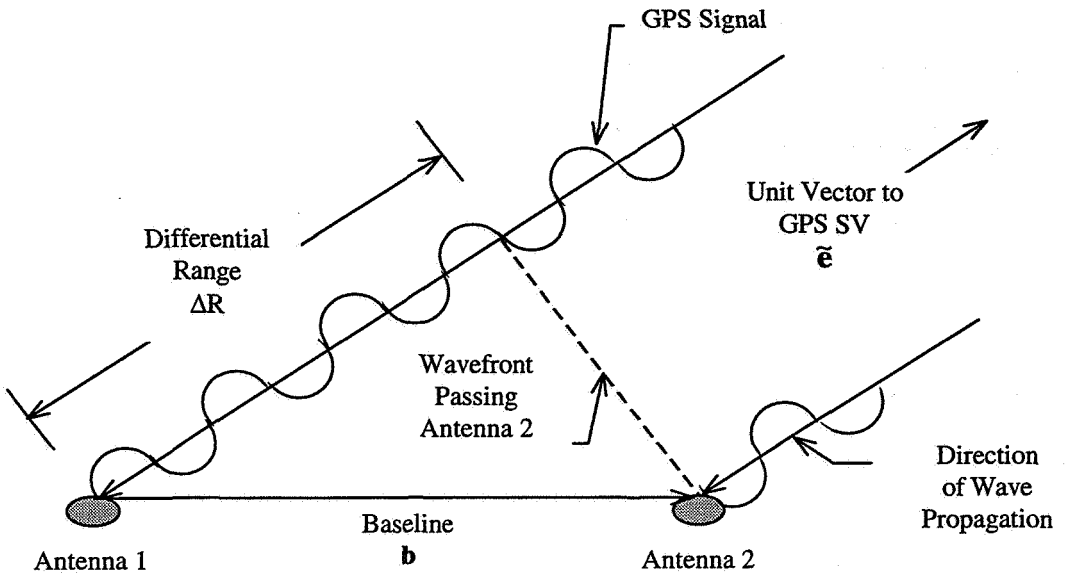

Figure 1: Differential Phase Geometry

may be expressed in cycles by dividing the result by λ, the wavelength of the L1 GPS carrier signal[10]:

$$\Delta R_{ij} = \frac{\mathbf{b}_i \cdot \tilde{\mathbf{e}}_j}{\lambda} \tag{4}$$

In this example, after the wave crosses Antenna 2, three and a half cycles are completed before the wavefront reaches Antenna 1. The range difference may therefore be decomposed into integer and fractional parts:

$$\Delta R_{ij} = k_{ij} + \Delta\varphi_{ij}. \tag{5}$$

The first term k_{ij} is known as the integer ambiguity. The second term $\Delta\varphi_{ij}$ is the fractional difference in phase cycles and is referred to as the differential phase. Solving for this differential phase using Equations 4 and 5 gives the result

$$\Delta\varphi_{ij} = \Delta R_{ij} - k_{ij} = \frac{\mathbf{b}_i \cdot \tilde{\mathbf{e}}_j}{\lambda} - k_{ij} \qquad (6)$$

In a working environment, noise will corrupt differential phase measurements, rendering Equation 6 incomplete. A portion of this noise is due to line bias and is treated as a separate term. Adding, then, a line bias β_i for each baseline and a noise term μ_{ij} to Equation 6 gives

$$\Delta\varphi_{ij} = \frac{\mathbf{b}_i \cdot \tilde{\mathbf{e}}_j}{\lambda} - k_{ij} + \beta_i + \mu_{ij} \qquad (7)$$

The line bias results from the finite time delay as measurement signals travel from the antenna to the GPS receiver. Therefore, the line bias is independent of the SV's. However, environmental conditions such as temperature might affect the electrical properties of the transmission line. The line bias is assumed to have a range of (-1,1) because an absolute value greater than or equal to one would be indistinguishable from the integer count number k_{ij}.

For the moment, consider perfect (noise-free) conditions such that Equation 6 applies. At one instant of time, differential phase measurements from three SV's are necessary to determine the baseline vector in the inertial frame assuming the integer ambiguities for each satellite are known. For example, the measurement equations for one baseline may be written as

$$\begin{bmatrix} \Delta\varphi_1 \\ \Delta\varphi_2 \\ \Delta\varphi_3 \end{bmatrix} = \frac{1}{\lambda}\begin{bmatrix} e_{1x} & e_{1y} & e_{1z} \\ e_{2x} & e_{2y} & e_{2z} \\ e_{3x} & e_{3y} & e_{3z} \end{bmatrix}\begin{bmatrix} b_x \\ b_y \\ b_z \end{bmatrix} - \begin{bmatrix} k_1 \\ k_2 \\ k_3 \end{bmatrix} \tag{8}$$

where the rows of the 3x3 matrix are the unit vectors to SV numbers 1, 2, and 3, respectively. Equation 7 may also be expressed as

$$\begin{aligned} \lambda(\Delta\varphi_1 + k_1) &= e_{1x}b_x + e_{1y}b_y + e_{1z}b_z \\ \lambda(\Delta\varphi_2 + k_2) &= e_{2x}b_x + e_{2y}b_y + e_{2z}b_z \\ \lambda(\Delta\varphi_3 + k_3) &= e_{3x}b_x + e_{3y}b_y + e_{3z}b_z \end{aligned} \tag{9}$$

which emphasizes that this is a system with three equations and three unknowns: the x, y, and z components of the baseline **b**.

The fact that the integers are known is a fair assumption in two cases: the baseline vector is either known to within a wavelength or is known to be less than one wavelength in length, for which case the integers are all zero. Regardless, only a small vector correction is sought. The former case will be examined in Section 3.2, Residual Formation. If the baselines are completely unknown, however, the integers must be determined with the baseline components. One approach is to take measurements at two time indices for the same three SV's. This gives six equations and three unknowns since the fixed attitude causes the integers to be constant over short periods of time. Over longer periods, the integer ambiguities simply increase or decrease by one each time the differential phase completes a cycle. For the most general situation, baseline motion must also be taken into account. Allowing for motion between the first and second measurement epochs introduces three more position vector components to the list of

unknowns. This can be overcome by taking measurements from six SV's at two measurement epochs. The complete system of twelve equations involves the following twelve unknowns: three baseline components at the first epoch, three baseline components at the second epoch, and six integer ambiguities. Any standard approach to solving a system of linear equations may then be employed. Noisy data will, however, require that more measurements be taken. Any number of filters can be used to extract the necessary baseline data from noisy measurements. A batch least-squares filter will be discussed in Section 3.2, Residual Formation. In Chapter 5, a sequential Kalman filter is used for continuous attitude determination on-board the TRACE spacecraft.

After solving two sets of equations such as in Equation 8 for two different baselines in the inertial frame, Equations 1 and 2 may be used to form the transformation matrix ${}^{B}\mathbf{C}^{I}$. This gives, finally, the attitude of the spacecraft with respect to the inertial frame.

2.2 Kalman Filter Equations

The Kalman filter is a sequential filter with the advantages of weighting factors on measurements and filter solution propagation. In other words, by correctly "tuning" the filter, proper balance can be achieved between data measurements and state noise. This allows one to selectively determine the degree to which the filter's solution will track the incoming measurements or the degree of data smoothing which will occur[11].

The quantity to be determined in Kalman filtering is the estimated state $\hat{\mathbf{x}}$ of the system, the true state of which is given by $\mathbf{x}$. Associated with this estimate is an error covariance matrix $\mathbf{P}$. To begin the Kalman filter process, an *a priori* estimate of the state

and its covariance matrix must be made. During each iteration of the filter, a weighting factor known as the Kalman gain **K** is formed. This gain is used to update the estimate of the state and covariance, forming the best estimate of these quantities from the available observations. With knowledge of the dynamics of the system, the estimated state and covariance are propagated forward to serve as the *a priori* estimate for the next iteration, and the process begins again. The flow chart of Figure 2 illustrates the iterative nature of the solution.

The state equations upon which the Kalman filter method is based are the dynamics model and the measurement model equations. The dynamics of the system are embodied in the state transition matrix Φ, which enables us to write

$$\mathbf{x}(n) = \Phi(n, n-1)\mathbf{x}(n-1) + \mathbf{w}(n-1) \tag{10}$$

This simply relates the state of the system at the n^{th} time step to the previous state plus a noise term **w**. This noise term is assumed to have the characteristics of white noise. Therefore, the mean of the noise is zero:

$$\mathrm{E}[\mathbf{w}(n)] = 0 \tag{11}$$

and there is no correlation between its elements at different times. However, there may be some correlation among the measurement elements at any one time. Thus the state noise covariance matrix **Q** satisfies the relation

$$\mathrm{E}\left[\mathbf{w}(m)\mathbf{w}(n)^{\mathrm{T}}\right] = \mathbf{Q}(n)\delta_n^m \tag{12}$$

where δ_n^m is the Kronecker delta function.

The measurement model equation for use in the Kalman filter relates the measurements to the state of the system. The observation matrix **H** is used to express the relationship:

$$\mathbf{z}(n) = \mathbf{H}(n)\mathbf{x}(n) + \mathbf{v}(n). \tag{13}$$

Here, **z** is the measurement vector and **v** is the associated noise, assumed to be white. The observation matrix is formed by taking the derivatives of the observations with respect to the variables in the state estimate. The covariance matrix associated with the

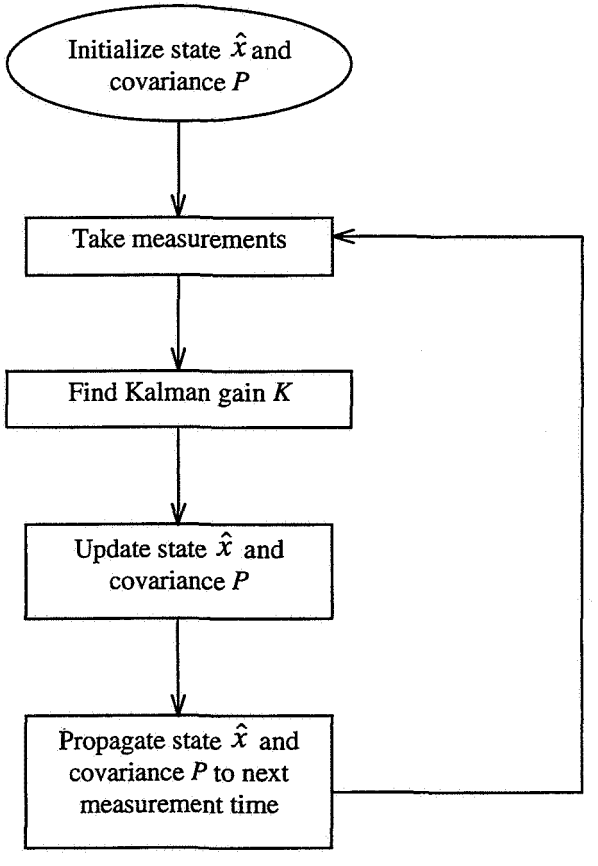

Figure 2: Kalman Filter Iterative Solution

measurement noise satisfies the relation:

$$\mathrm{E}\left[\mathbf{v}(m)\mathbf{v}(n)^{\mathrm{T}}\right] = \mathbf{R}(n)\delta_n^m. \tag{14}$$

The proper formation of this quantity is quite important in the filtering process. Studying actual measurement data will enable the formation of an accurate measurement model for use in the filter.

Now that all the terms have been defined, the equations used in the Kalman filter may be presented. After the measurements have been made and the observation matrix determined, the Kalman gain is computed using the following equation[12]:

$$\mathbf{K}_n = \mathbf{P}_n^- \mathbf{H}_n^{\mathrm{T}} \left(\mathbf{H}_n \mathbf{P}_n^- \mathbf{H}_n^{\mathrm{T}} + \mathbf{R}_n\right)^{-1}. \tag{15}$$

Here, the subscript n signifies the n^{th} time step and the superscript (-) indicates an *a priori* estimate propagated from the last time step and made before the current measurement.

Once the Kalman gain has been found, the state is updated for the current observation using

$$\hat{\mathbf{x}}_n^+ = \hat{\mathbf{x}}_n^- + \mathbf{K}_n\left(\mathbf{z}_n - \mathbf{H}_n\hat{\mathbf{x}}_n^-\right), \tag{16}$$

and the state covariance $\mathbf{P}$ is updated with the equation

$$\mathbf{P}_n^+ = \left(\mathbf{I} - \mathbf{K}_n\mathbf{H}_n\right)\mathbf{P}_n^-\left(\mathbf{I} - \mathbf{K}_n\mathbf{H}_n\right)^{\mathrm{T}} + \mathbf{K}_n\mathbf{R}_n\mathbf{K}_n^{\mathrm{T}}. \tag{17}$$

The superscript (+) in these equations indicates a quantity after being updated with measurement information. The pre- and post-multiplication by the quantity in parentheses is performed to preserve the symmetry of the covariance matrix.

To propagate the state and the covariance to the next time step, the state transition matrix Φ is used:

$$\hat{\mathbf{x}}_{n+1}^{-} = \Phi(n+1,n)\hat{\mathbf{x}}_n \tag{18}$$

$$\mathbf{P}_{n+1}^{-} = \Phi(n+1,n)\mathbf{P}_n\Phi(n+1,n)^{\mathrm{T}} + \mathbf{Q}_n. \tag{19}$$

These two equations produce the *a priori* estimates which will be used to start the next iteration of the Kalman filter.

3. Noise Model Development

In order to perform more realistic simulations for GPS attitude determination, it is necessary to have a noise model for the differential phase measurements. After extensive analysis of data provided by NASA Johnson Space Flight Center (JSC), the development of a such a noise model for the differential phase was possible. The differences between observed and calculated differential phase measurements provided measurement errors upon which the noise model was built.

Data from two separate experiments conducted at JSC are examined in this chapter. GPS measurements are known to be susceptible to multipath, a phenomenon which occurs when the direct GPS signal is corrupted by indirect signals reflected off surrounding surfaces[13]. One of the experiments was designed to limit the effects of multipath by placing the antennas in an open field. The other experiment took place on a rooftop, where numerous metal surfaces provided sources for multipath reflection. Both experiments, however, used the same GPS receiver and mounting table for the antennas. The methods used to determine the differential phase noise model will be demonstrated with the rooftop data. A comparison of the rooftop and field data results will then be made.

3.1 Rooftop Experiment Description

The rooftop experiment consists of four GPS antennas arranged in a pyramid configuration and placed upon an optical bench on a rooftop (see Figure 3). Because the configuration is static and earth-bound, the attitude is described in an Earth-Centered Earth-Fixed (ECEF) reference frame rather than Earth-Centered Inertial. The baselines

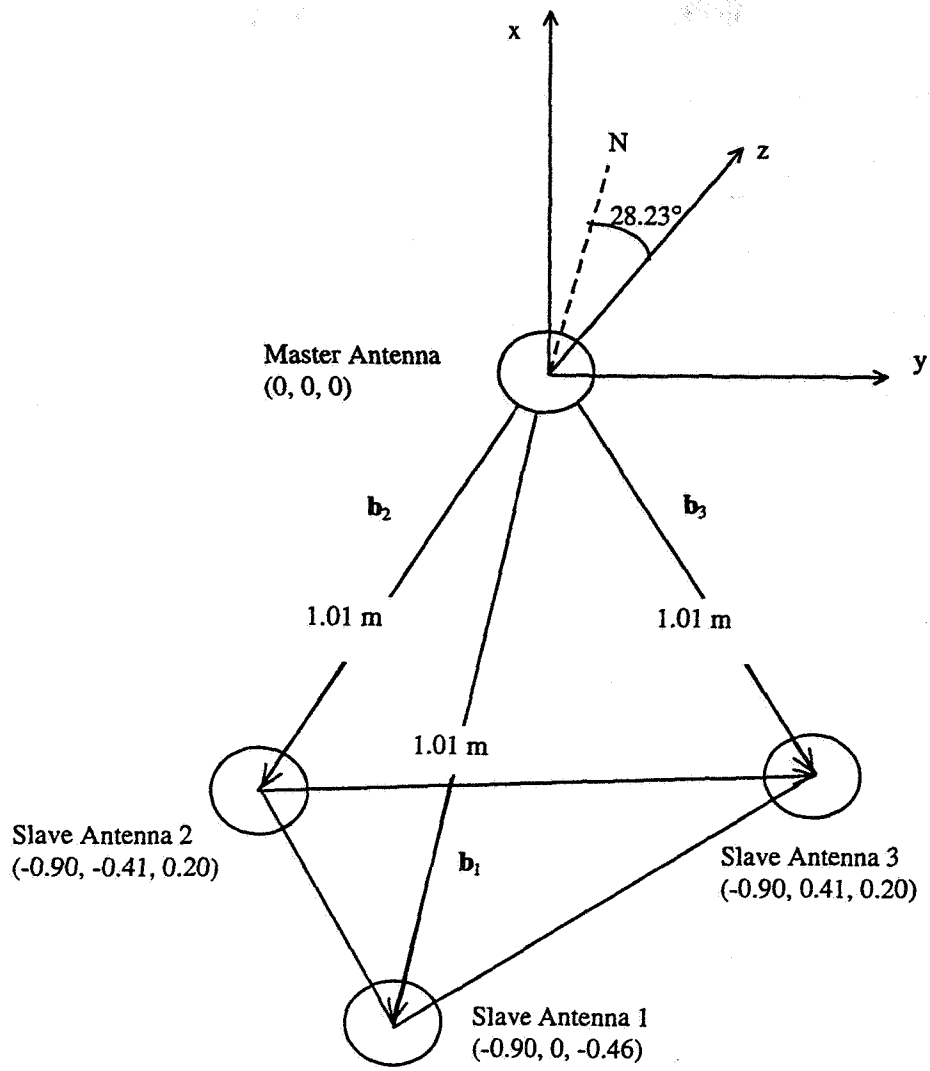

Figure 3: Rooftop GPS Antenna Configuration Showing Body Frame Coordinates

are known within 2-3 centimeters in the body reference frame and are shown in the figure (private communication, Penny Saunders, NASA JSC). The transformation matrix ${}^{E}\mathbf{C}^{B}$ corresponding to the known attitude is used to write the baselines in the ECEF system:

$$\mathbf{b}_i \equiv \mathbf{b}_i^E = {}^{E}\mathbf{C}^{B}\mathbf{b}_i^B \qquad (20)$$

The GPS receiver used is the Trimble TANSQuad, a single receiver designed to provide differential phase measurements from four separate antennas. With this receiver, one antenna is designated as the master and the remaining three serve as slave antennas. L1 carrier phase measurements are made for each of the antennas. To form these carrier phase measurements, the receiver starts a count at some large negative number and increases the count for every wavelength received. The differential phase is then formed by differencing these carrier phase counts between the master and each of the slaves. Because the difference is formed from only one receiver, no errors associated with the clock of the receiver are present[14].

The master antenna is located at the apex of the arrangement, and the three slave antennas form the base. The baselines extend from master to slave, as depicted in Figure 3. The body coordinate system places the master at the origin. The coordinates of the slaves are thus the baseline vector coordinates and are expressed in the figure in meters.

Twelve GPS satellites were in view over the four and a half hour data collection period. Figure 4 shows the SV coverage as a function of azimuth and elevation angles. The center of the graph is at an elevation angle of 90° and the horizon is at the outer edge. There is good coverage except for low elevations near 0° azimuth.

3.2 Residual Formation

The first step in forming the noise model was to reduce the GPS differential phase measurements reported by the receiver to a set of error residuals, represented by the noise term μ_{ij} in Equation 7. Using unit vectors to the SV's expressed in the same ECEF reference frame as the known attitude, the differential phase as given by Equation 7 is

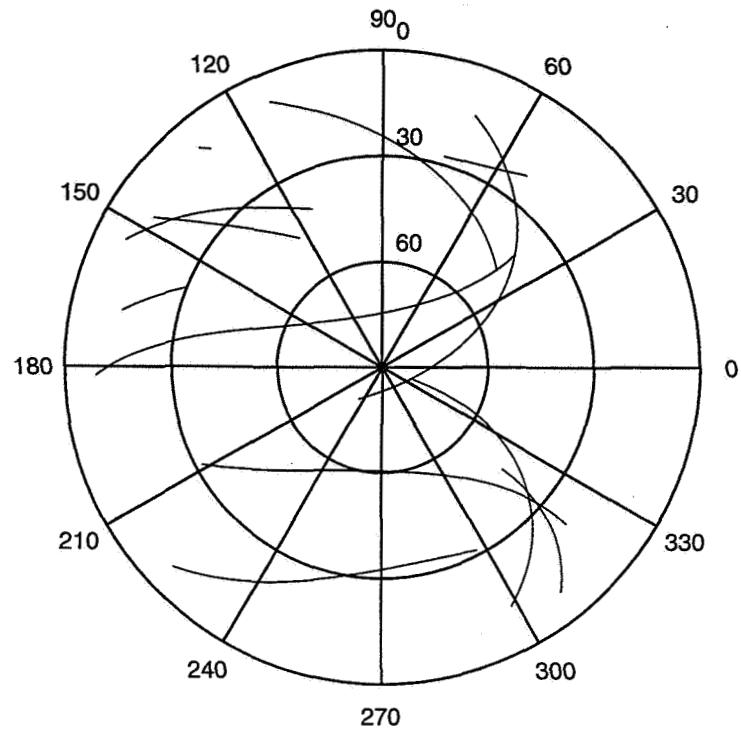

Figure 4: SV Coverage Showing Azimuth and Elevation

$$\Delta\varphi_{ij} = \frac{\mathbf{b}_i \cdot \tilde{\mathbf{e}}_j}{\lambda} - k_{ij} + \beta_i + \mu_{ij} \qquad (21)$$

where $\mathbf{b}_i$ is given by Equation 20. As before, the subscript i refers the i^{th} baseline and the subscript j refers to the j^{th} SV. Since the baselines are known to within 2-3 cm, less than the 19 cm wavelength of the L1 carrier signal, the integer ambiguities are known. However, small corrections to the baselines may be necessary and must be determined. In addition, the unknown line biases must be computed.

The first estimate of the differential phases assumes that the baselines are correct and that there are no line biases or noise. Thus Equation 6 is used to write

$$\Delta\hat{\varphi}_{ij} = \frac{\hat{\mathbf{b}}_i \cdot \tilde{\mathbf{e}}_j}{\lambda} - k_{ij} \qquad (22)$$

where the hat over the baseline vector indicates that it is an estimated value. Figure 5 and Figure 6 show the differential phase measurements $\Delta\varphi_{ij}$ reported by the JSC receiver for representative SV's using all three baselines. Also included in the graphs are the estimates of the differential phases calculated from Equation 22. Each observation and calculation pair is distinguished by a different line type in the figures. The calculated signal, since it has no noise, is the smoother of each pair.

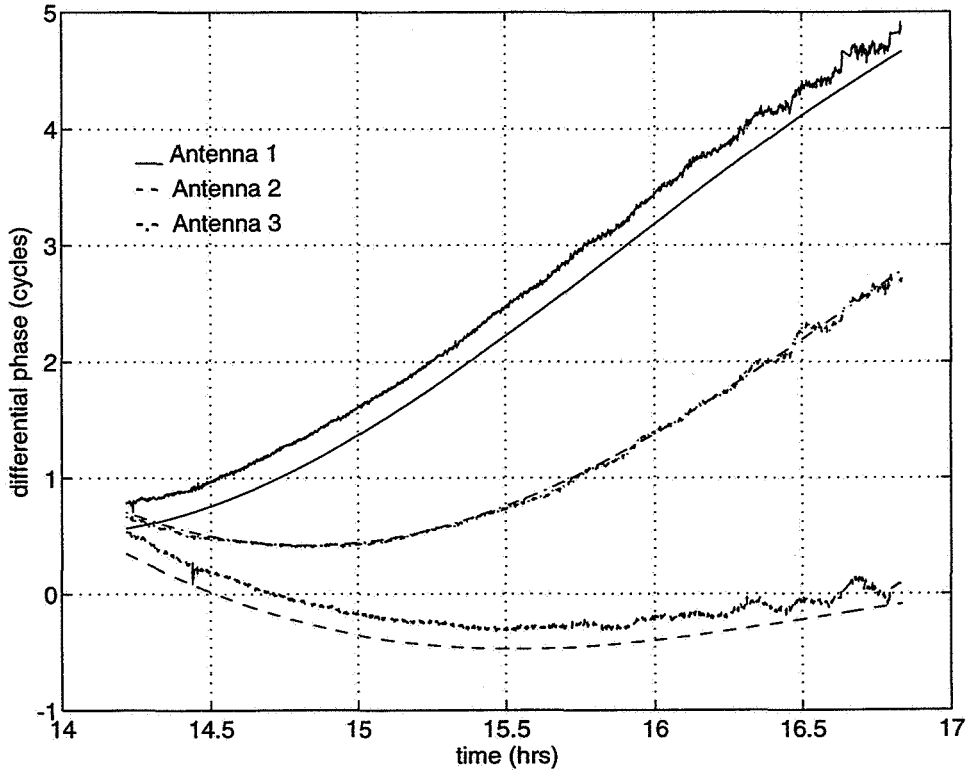

Figure 5: SV15 Differential Phase Observations and Calculations

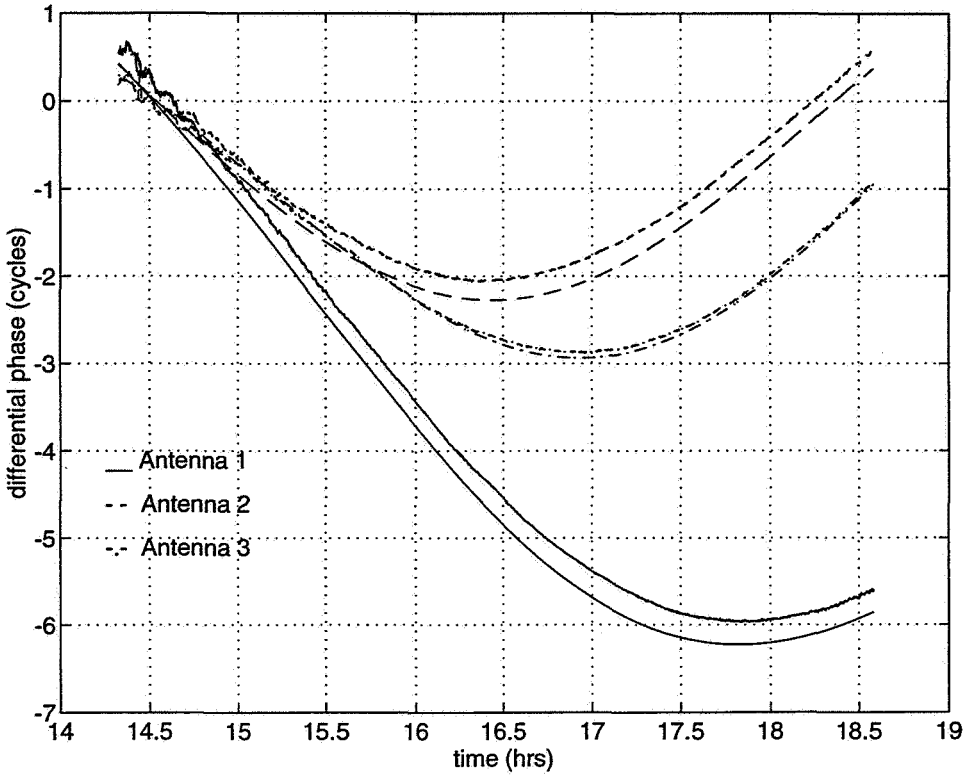

Figure 6: SV22 Differential Phase Observations and Calculations

The differential phase residuals, designated by $\delta\Delta\varphi$, are computed by taking the observed minus the calculated differential phase measurements, or Equation 21 minus Equation 22:

$$\begin{aligned}\delta\Delta\varphi_{ij} &= \Delta\varphi_{ij} - \Delta\hat{\varphi}_{ij} \\ &= \frac{\left(\mathbf{b}_i - \hat{\mathbf{b}}_i\right)\cdot \tilde{\mathbf{e}}_j}{\lambda} + \beta_i + \mu_{ij} \\ &\equiv \frac{\delta\mathbf{b}_i \cdot \tilde{\mathbf{e}}_j}{\lambda} + \beta_i + \mu_{ij}\end{aligned} \qquad (23)$$

The differential phase residuals for the previously used SV's are plotted in Figure 7 and Figure 8. The lines biases appear in these graphs as constant offsets: roughly 0.25, 0.2, and 0 cycles for antennas 1, 2, and 3, respectively in both figures. Approximately the same offsets are seen across all SV's. This supports the contention that the line biases are inherent in the receiver and can therefore be represented in the differential phase equation by the constant line bias term β_i. Noise is corrupting the signal and can be seen in the figures as well. The effect of the baseline errors is most easily seen in Figure 8, in which a clear trend is seen in the data that is the similar for all three antennas.

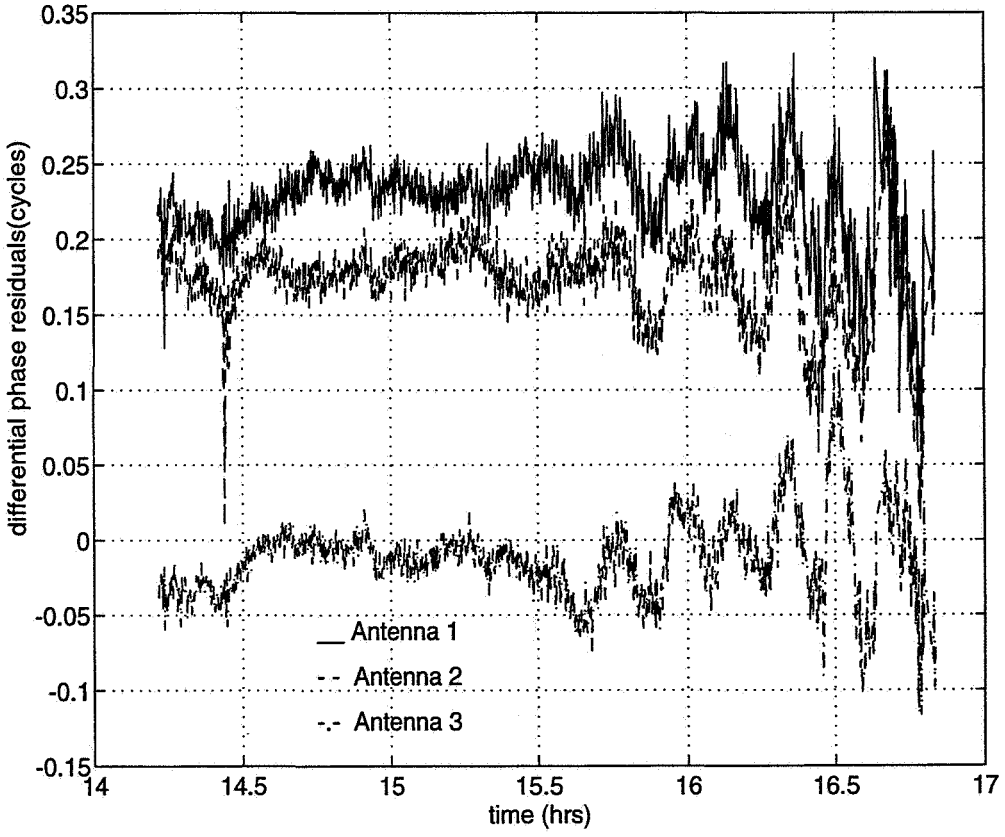

Figure 7: SV15 Differential Phase Residuals

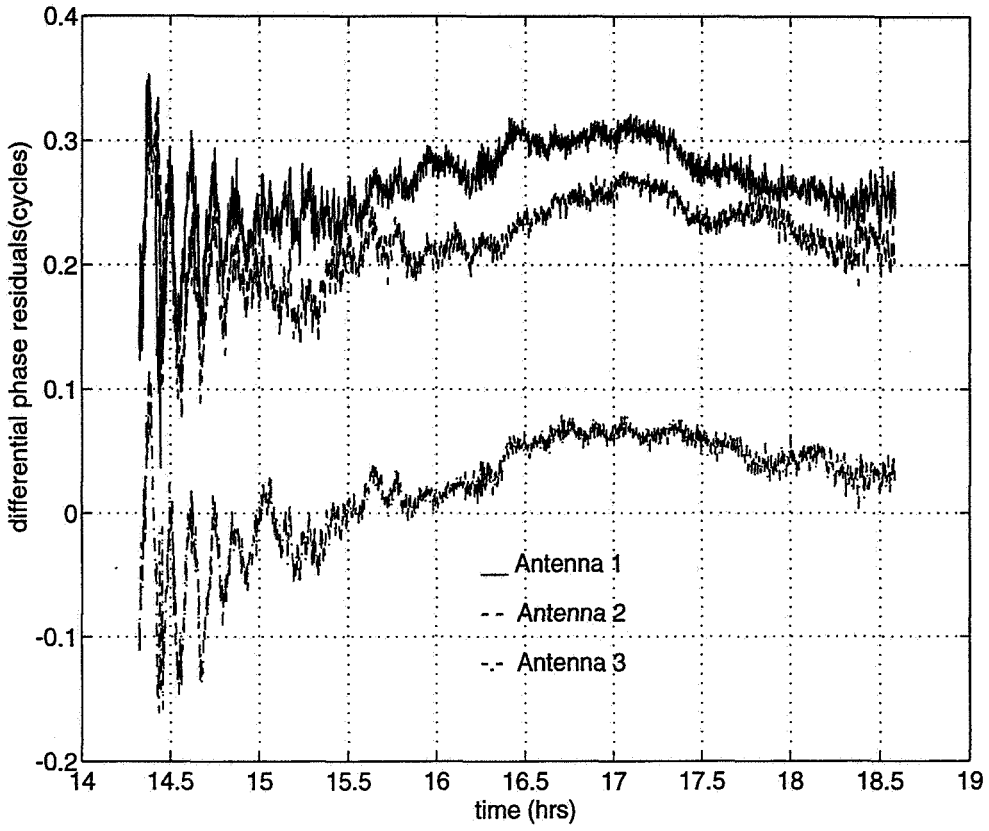

Figure 8: SV22 Differential Phase Residuals

To obtain the best estimate of the baselines in the ECEF frame and also to solve for the line biases, the differential phase residuals $\delta\Delta\varphi_{ij}$ are used in a least-squares batch filter. The changes in the baseline vectors and the line biases associated with each baseline comprise the state vector **x** to be determined. Since the differential phase measurements from each antenna are independent, the baselines corrections and line biases may be determined separately for each baseline. For one baseline, the state vector is assumed to be constant in time and is given by

$$\mathbf{x} = \begin{bmatrix} \delta\mathbf{b} \\ \beta \end{bmatrix} = \begin{bmatrix} \delta b_x \\ \delta b_y \\ \delta b_z \\ \beta \end{bmatrix} \tag{24}$$

The observation matrix is formed by taking the derivative of Equation 23 with respect to each of the state elements. Since the GPS constellation is changing with time, the observation matrix at one measurement epoch t_k is given by

$$\mathbf{H}_j(t_k) = \begin{bmatrix} e_{jx}(t_k) & e_{jy}(t_k) & e_{jz}(t_k) & 1 \end{bmatrix} \tag{25}$$

This observation matrix is the same for all three baselines. Putting the state and observation matrices in Equation 23 gives the matrix form of the system at one measurement epoch t_k for the SV j:

$$\delta\Delta\varphi_j(t_k) = \mathbf{H}_j(t_k)\mathbf{x} \tag{26}$$

To perform the least-squares fit, measurements from all twelve observable SV's for each measurement epoch are concatenated into one measurement vector. Thus for one baseline, the full matrix form of the system is

$$\begin{bmatrix} \delta\Delta\varphi_1(t_1) \\ \delta\Delta\varphi_1(t_2) \\ \delta\Delta\varphi_1(t_3) \\ \vdots \\ \hline \delta\Delta\varphi_2(t_1) \\ \delta\Delta\varphi_2(t_2) \\ \vdots \end{bmatrix} = \begin{bmatrix} \mathbf{H}_1(t_1) \\ \mathbf{H}_1(t_2) \\ \mathbf{H}_1(t_3) \\ \vdots \\ \hline \mathbf{H}_2(t_1) \\ \mathbf{H}_2(t_2) \\ \vdots \end{bmatrix} \mathbf{x} \tag{27}$$

which will be defined as

$$\mathbf{z} = \mathbf{H}\mathbf{x} \tag{28}$$

Using the pseudo-inverse of **H**, the least-squares solution of the system is given by

$$\hat{\mathbf{x}} = \left(\mathbf{H}^{\mathrm{T}}\mathbf{H}\right)^{-1}\mathbf{H}^{\mathrm{T}}\mathbf{z} \tag{29}$$

The system given in Equation 27 is solved for each of the three measurement vectors **z** corresponding to the three baselines. The resulting baseline corrections and line biases are shown in Table 1. The total length of the adjustments made to each baseline are about 2 cm, which is consistent with independent results obtained by JSC researchers.

The differential phase estimate in Equation 22 may now be improved by including

	Baseline 1	Baseline 2	Baseline 3
Line Bias (cycles)	0.19	0.14	-0.05
Δx (cm)	-0.25	-0.08	-0.14
Δy (cm)	-1.70	-1.85	-1.65
Δz (cm)	1.01	0.88	1.14
Total Length of Baseline Correction (cm)	**1.99**	**2.05**	**2.01**

Table 1: Baseline Corrections and Line Biases Resulting from Least-Squares Fit

the baseline corrections and line biases:

$$\Delta\hat{\varphi}_{ij} = \frac{\left(\hat{\mathbf{b}}_i + \delta\mathbf{b}_i\right)\cdot\tilde{\mathbf{e}}_j}{\lambda} - k_{ij} + \beta_i. \qquad (30)$$

When these newly calculated differential phases are plotted against the observations, the agreement is seen to be quite good (See Figure 9). If this improved estimate of the differential phase is subtracted from Equation 21, the result is a residual set which contains only the noise term μ_{ij}:

$$\begin{aligned} \delta\Delta\varphi_{ij} &= \Delta\varphi_{ij} - \Delta\hat{\varphi}_{ij} \\ &= \frac{\left\{\mathbf{b}_i - \left(\hat{\mathbf{b}}_i + \delta\mathbf{b}_i\right)\right\}\cdot\tilde{\mathbf{e}}_j}{\lambda} + \mu_{ij} \\ &\approx \mu_{ij} \end{aligned} \qquad (31)$$

Figure 10 shows the improved residual set which results from the least-squares fit for one of the two SV's. The curves lie atop one another, demonstrating the quality of the fit. The errors which remain are likely the result of multipath interference due to reflections off the metallic roof approximately 2 meters below the master.

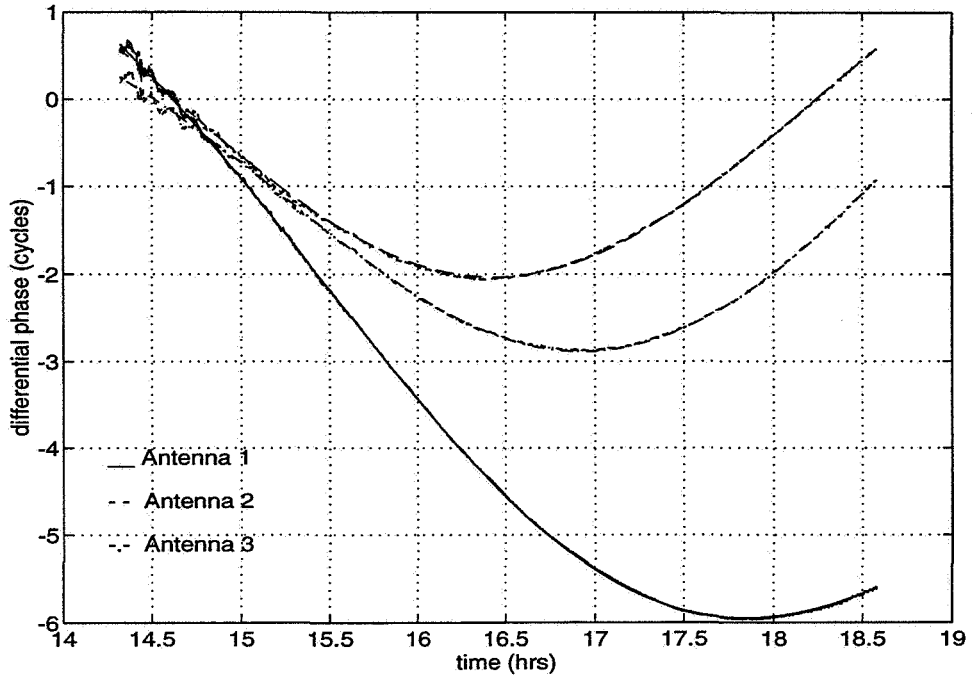

Figure 9: SV22 Differential Phase Observations and Calculations after Least-Squares

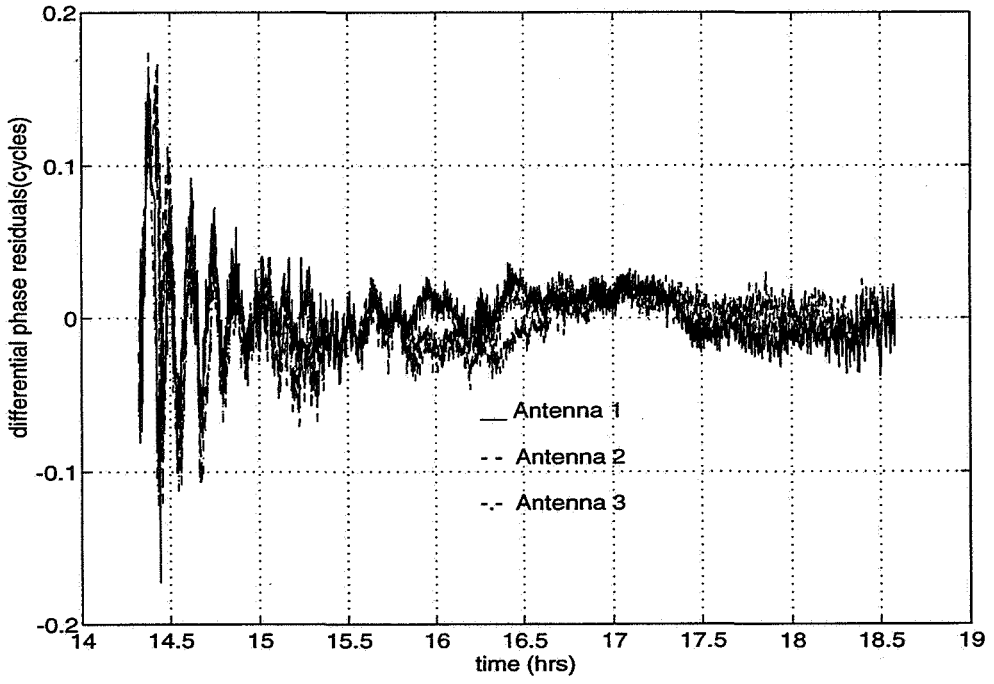

Figure 10: SV22 Differential Phase Residuals after Least-Squares

3.3 Noise Model Identification

The goal of this section is to develop a model of the differential phase errors. One method for doing this is system identification, an analysis tool that uses the observed input and output of a system to estimate a model for the system. Using this method, the differential phase residuals resulting from the previous section are analyzed statistically. The model that results is used to produce statistically equivalent pseudodata for use in attitude determination simulations.

3.3.1 Data Preparation

Because the method is based on the statistics of the data, several steps were necessary to prepare the data for time-series analysis. The first step was to resample the data at a uniform rate. A non-uniform sampling rate was used by the GPS receiver at JSC: data for each satellite was reported at sampling intervals that varied by multiples of half a second. However, an analysis of the sampling rate distribution showed that 2.5 seconds was the most common sampling interval: fully 80% of the sampling was done with this interval. This rate was used as the fixed sampling interval in a linear interpolation of the data, resulting in a time series of uniform sampling rate f equal to 0.4 Hz for each of the satellites. Hence, for each satellite j the differential phase residuals are of length

$$n_j = T_j f \tag{32}$$

where T_j is the total period of time over which the satellite is in view.

An important criteria in time series analysis is that the data be stationary, meaning the statistics of the data do not change over time. For the purposes of this study, weak stationarity will be sufficient. To satisfy this requirement, only the mean and variance of

the data must be nearly constant over time[15]. An examination of Figure 10 reveals large oscillations prior to 15 hours for each baseline. Figure 11(a) shows the residuals for another sample satellite, SV14. For this satellite, the largest oscillations occur before 15.5 hours. As mentioned previously, these errors are probably the result of multipath. The elevation plot shown in (b) of the same figure suggests that the multipath corruption is greatest at low elevations. This trend holds true across all twelve of the SV's examined. An elevation of 30° is therefore chosen as the cutoff angle below which the data is eliminated from the data set. The differential phase error model will concentrate only on the effects seen at higher elevations. The vertical dashed lines of Figure 11(b) show the limits of the data kept from this particular residual set. Between these lines the elevation is greater than 30°.

After eliminating the data at low elevations, the residual series are improved but not yet weakly stationary. The low frequency components of the differential phase residuals apparent in the center of Figure 11(a) destroy the stationarity of short time series associated with individual SV's. However, as the number of data points increases, the data becomes more stationary, for the mean and variance taken over longer periods of time tend toward average values. Thus, by concatenating all of the SV differential phase time series into one single series, the stationarity requirement is more nearly met. The data for each antenna and for each SV are reduced to zero mean before concatenation to help reduce discontinuities between data sets. The combination of the individual data sets thus produces a single series of length

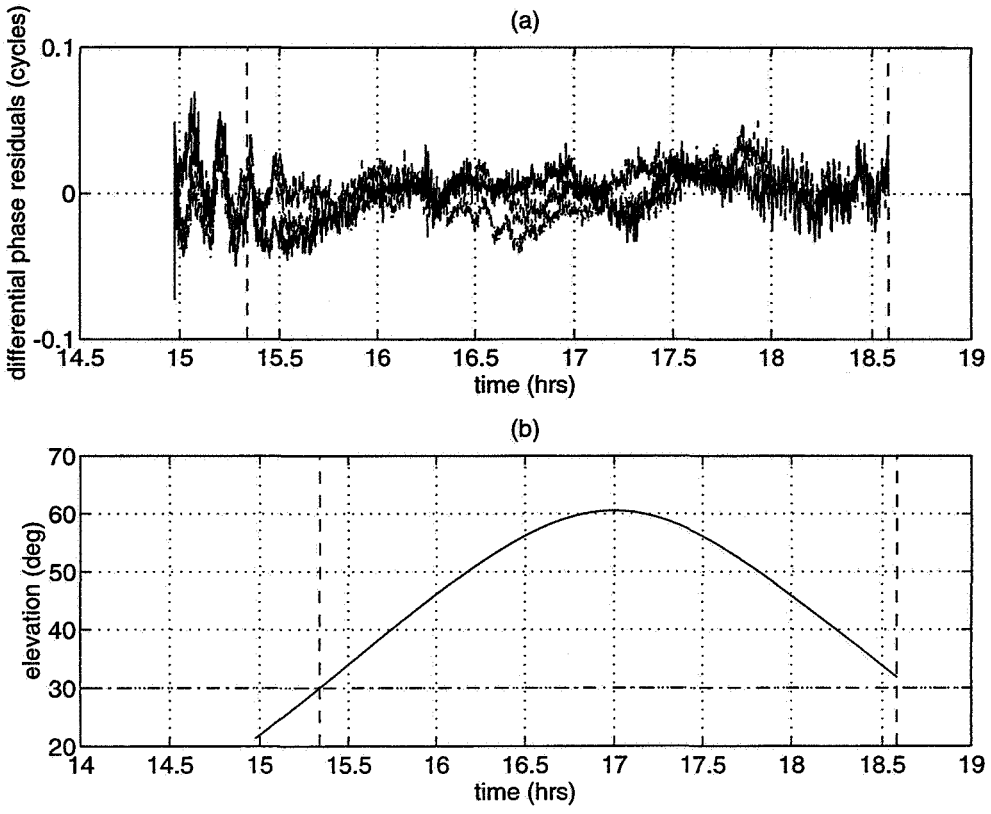

Figure 11: SV14 Elevation Angles and Differential Phase Residuals

$$N = \sum_j 3n_j \tag{33}$$

since data for all three baselines is available for each SV. The series so formed will be referred to as $z(t_k)$. It is exactly analogous to the observation vector **z** found in the least-squares development of Section 3.2, Residual Formation. Here, the process has been taken one step further to concatenate the data from all three baselines into one series. Furthermore, the improved residual set of Equation 31 is used, which contains only the noise to be modeled.

3.3.2 Shaping Filter Overview

The residual series resulting from the data preparation is not white noise. By analyzing this data with system identification methods, a model to reproduce the statistical characteristics apparent in the signal may be developed. Following the example of Braasch[16], a filter G was designed to reduce the residual data $z(t_k)$ of length N to white noise. Such a filter is depicted in Figure 12. In this case, $e(t_k)$ is white noise of zero mean and some variance.

The output of the linear filter G may be expressed in the frequency domain as

$$E(\omega) = G(\omega)Z(\omega) \tag{34}$$

where $E(\omega)$ and $Z(\omega)$ are the discrete Fourier transforms of $e(t_k)$ and $z(t_k)$, respectively. The inverse may therefore be written as

$$Z(\omega) = G^{-1}(\omega)E(\omega) \tag{35}$$

Now, white noise is characterized by having equal power in all frequencies. In a power spectral density (PSD) plot, white noise appears as a constant in frequency. The power in this frequency is determined by the variance of the noise. Thus, by choosing a different white noise sequence $e'(t_k)$ with the same variance as $e(t_k)$, the same frequency function

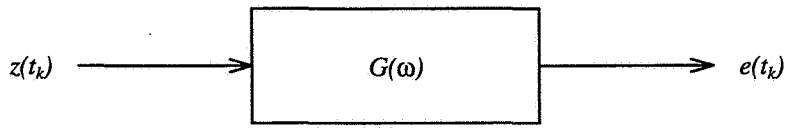

Figure 12: Filter for Reducing Residuals to White Noise

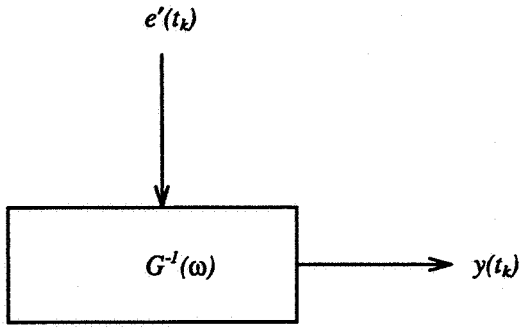

Figure 13: Shaping Filter

$E(\omega)$ will be obtained. Therefore, passing white noise of the same variance through the inverse filter G^{-1} results in data statistically equivalent to the original differential phase[17]. This process is shown in Figure 13. The output is a series $y(t_k)$ which has the same frequency characteristics as $z(t_k)$; i.e., $y(t_k)$ and $z(t_k)$ are both realizations of the same random process. Such a filter G^{-1} is called a shaping filter because it shapes white noise into the desired random process $y(t_k)$ (personal correspondence, *An Introductory Course on Kalman Filtering*, Joseph Garrick, NASA Goddard Space Flight Center).

The frequency-domain relationship between the random process $y(t_k)$ and some white noise signal $e(t_k)$ has the same form as Equation 36:

$$Y(\omega) = G^{-1}(\omega)E(\omega) \tag{36}$$

It is now assumed that G^{-1} may be represented by an auto-regressive moving-average, or ARMA, model structure. Equation 36 may thus be written as[18]

$$Y(\omega) \equiv \frac{C(\omega)}{A(\omega)} E(\omega) \tag{37}$$

or, equivalently

$$A(\omega)Y(\omega) = C(\omega)E(\omega) \tag{38}$$

where

$$A(\omega) = 1 + a_1 q^{-1} + \ldots + a_m q^{-m} \tag{39}$$

and

$$C(\omega) = 1 + c_1 q^{-1} + \ldots + c_n q^{-n}. \tag{40}$$

Furthermore, q^{-1} is the delay operator defined by

$$q^{-1} = e^{-i\omega\Delta t} \tag{41}$$

and where Δt=2.5 seconds is the sampling interval used in this study.

3.3.3 Model Selection

The coefficients of the polynomials $A(\omega)$ and $C(\omega)$ in Equations 39 and 40 are estimated using the System Identification Toolbox in MATLAB[19]. The polynomials that comprise the shaping filter are of order m and n, respectively. Given a combination of orders m and n and the signal $z(t_k)$ to be modeled, the MATLAB ARMAX function is used to determine the coefficients of the ARMA model. The function attempts to minimize the sum of the squares of the prediction error $e(t_k)$, which should be white. This is done with a Gauss-Newton minimization routine. Thus, for each choice of m and n, a different filter model, designated by $G^{-1}[m,n]$, is obtained. Then for each model, simulated differential phase error data $y(t_k)$ is produced by passing white noise of the appropriate variance through the shaping filter. This is accomplished with the MATLAB IDSIM

function. The resulting simulations are then compared to the original error signal $z(t_k)$. The model which produces a simulation most nearly matching $z(t_k)$ in a statistical sense and which has the "whitest" prediction error $e(t_k)$ is chosen as the best shaping filter model.

The first of two selection criteria used is the whiteness of the prediction error. Because white noise has equal power in all frequencies, the PSD of the prediction error for a given model must be flat. White noise is equivalently characterized by an autocorrelation function that is non-zero only at zero lag and has a value there equal to the variance of the noise. In other words, there is no correlation between any two data points in a white noise signal.

Because the model must reproduce the frequency characteristics of the differential phase residual signal, the PSD's of the observed signal and the simulated signal must be similar. This provides the second criterion for the quality of the fit of a given order shaping filter. Figure 14 compares the PSD's of two different models to that of the observed data $z(t_k)$. For each of the two models, the power spectra of both the prediction error $e(t_k)$, or ARMA residuals, of the model and the resulting simulation $y(t_k)$ are shown. As seen in the figure, the PSD of the prediction error corresponding to the $G^{-1}[5,4]$ model is much flatter than that of the $G^{-1}[2,2]$ model. In addition, the $G^{-1}[5,4]$ simulation spectrum mAtches the observAtion more closely than that of $G^{-1}[2,2]$. After mAny such comparisons for various orders of m and n, the $G^{-1}[5,4]$ shaping filter was determined to provide the best differential phase noise model. The equation for the chosen $G^{-1}[5,4]$ ARMA model shaping filter is given as

$$G^{-1}[5,4] = \frac{C(q)}{A(q)} = \frac{1 - 2.16q^{-1} + 1.29q^{-2} + 0.14q^{-3} - 0.25q^{-4}}{1 - 2.85q^{-1} + 2.82q^{-2} - 0.99q^{-3} - 0.05q^{-4} + 0.06q^{-5}} \qquad (42)$$

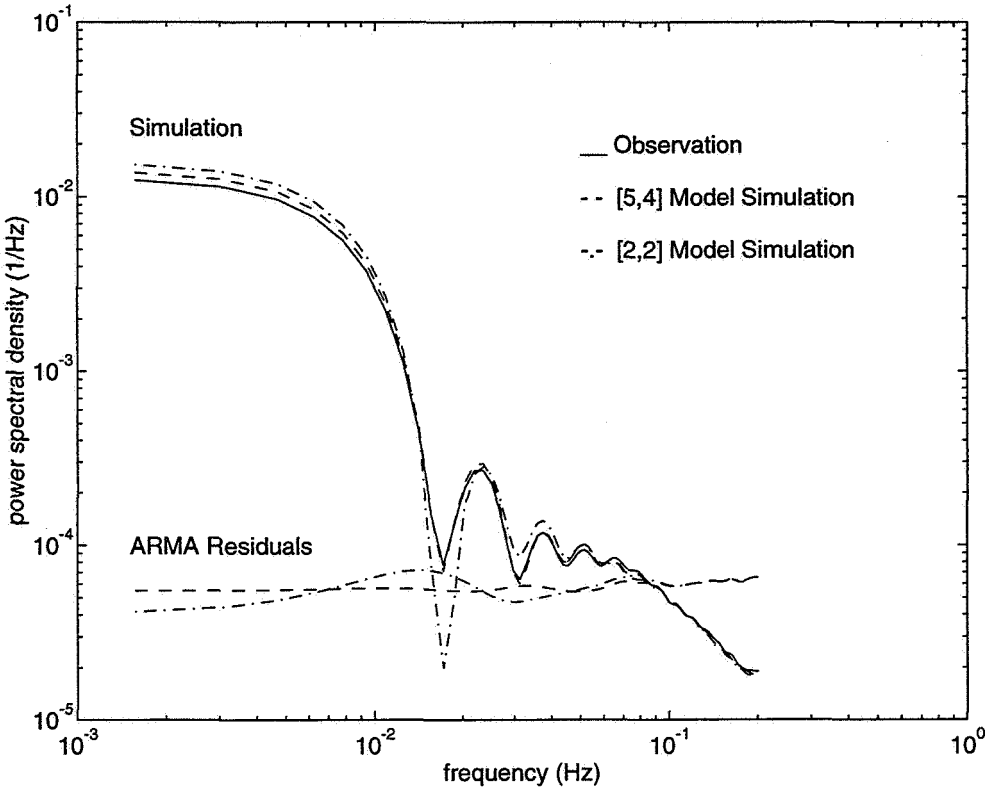

Figure 14: Comparison of Power Spectral Densities for Two ARMA Models

3.3.4 Simulating Differential Phase DAta

After choosing a suitable noise model for the differential phase residuals, simulated differential phase residual data may be formed by passing normally distributed white noise through the shaping filter, as described in the previous sections. Figure 15 compares the result of this simulation to the observed differential phase residuals for the satellite introduced in Section 3.3.1, Data Preparation. The top three plots are the residuals

collected from the three antennas. For clarity, the observations for antennas 1, 2, and 3 have been offset by 0.1, 0.2, and 0.3 cycles, respectively. The bottom plot, which is not offset, is the simulation that results from the error model. The actual shape of the simulation does not precisely match the observations because only statistically equivalent data has been produced, not a reproduction of the data itself. As mentioned previously, the simulation and observation are two realizations of the same random process. With this in mind, the similarities between the observations and simulation are quite apparent. The high frequencies are reproduced well, and some of the low frequencies, as seen near 17 hours in the figure, also appear in the simulation.

The real test of the noise model is made by comparing the power spectral density of the simulation obtained above to the PSD's obtained from each of the antenna observations. This comparison is shown in Figure 16. As expected, the simulation, designated by the solid line, lies mostly within the boundaries formed by the three observations. The PSD for antenna 3 for this particular SV happens to have less power particularly at about 0.018 Hz, but it matches the simulation well at the remaining frequencies. In effect, the simulation PSD is the "average" power spectral density for the SV in question. Using another random sequence to form the white noise would result in a slightly different simulation, and so the differences between the three antennas can be effectively modeled by running three simulations.

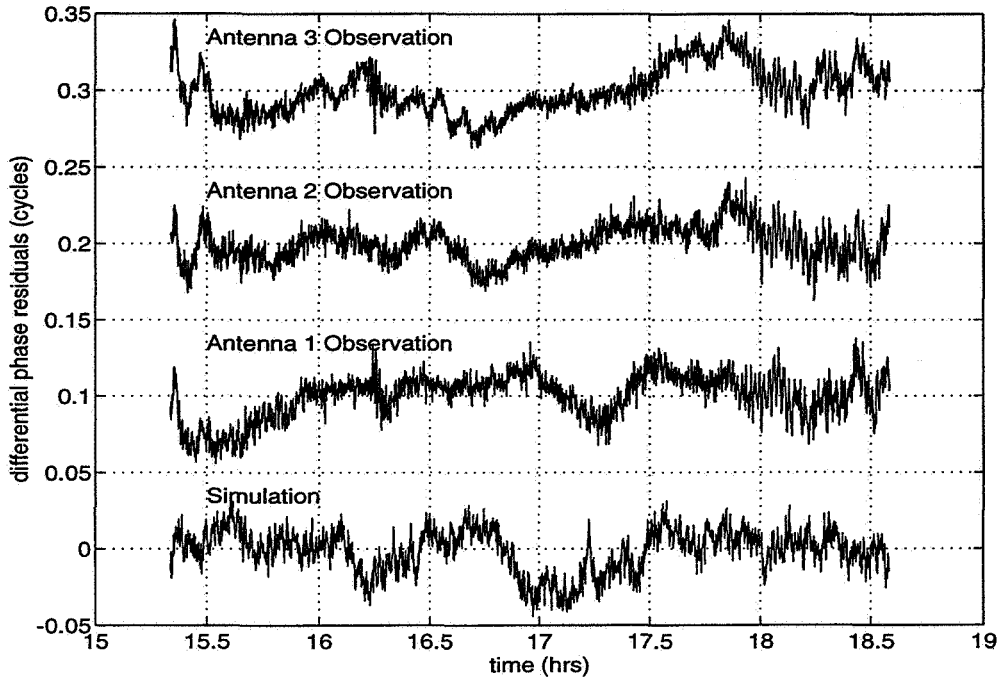

Figure 15: SV14 Observed and Simulated [5,4] Differential Phase Residuals

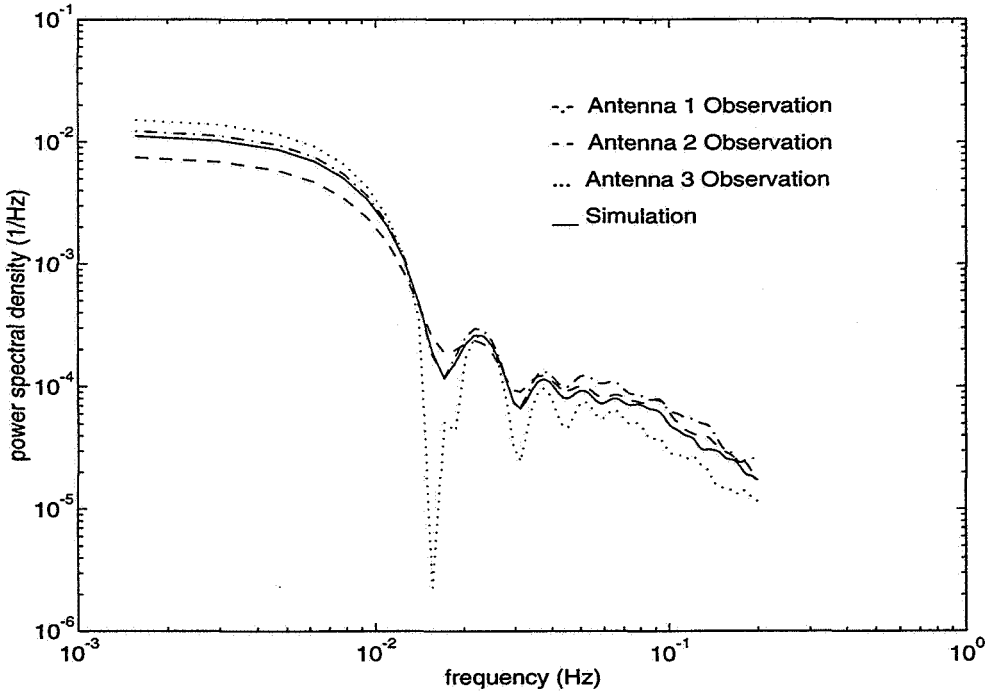

Figure 16: SV14 Observed and Simulated [5,4] Power Spectral Densities

3.3.5 Comparison of Rooftop and Field DAta

In the GPS experiment conducted in the field at JSC, all four antennas were placed flat on an optical bench, forming a two-foot square. Because the data was collected with the same Trimble TANSQuad receiver and antennas used on the rooftop, precisely the same analysis is performed as in the previous section to obtain the signal model.

When the power spectral densities of the field data are compared to those of the rooftop data, as demonstrated in Figure 17, it is seen that the shapes are similar but that the mAgnitudes of the spectra are lower in the field data. This is because fewer multipath reflectors were present in the open field than on the rooftop. In the graph, a

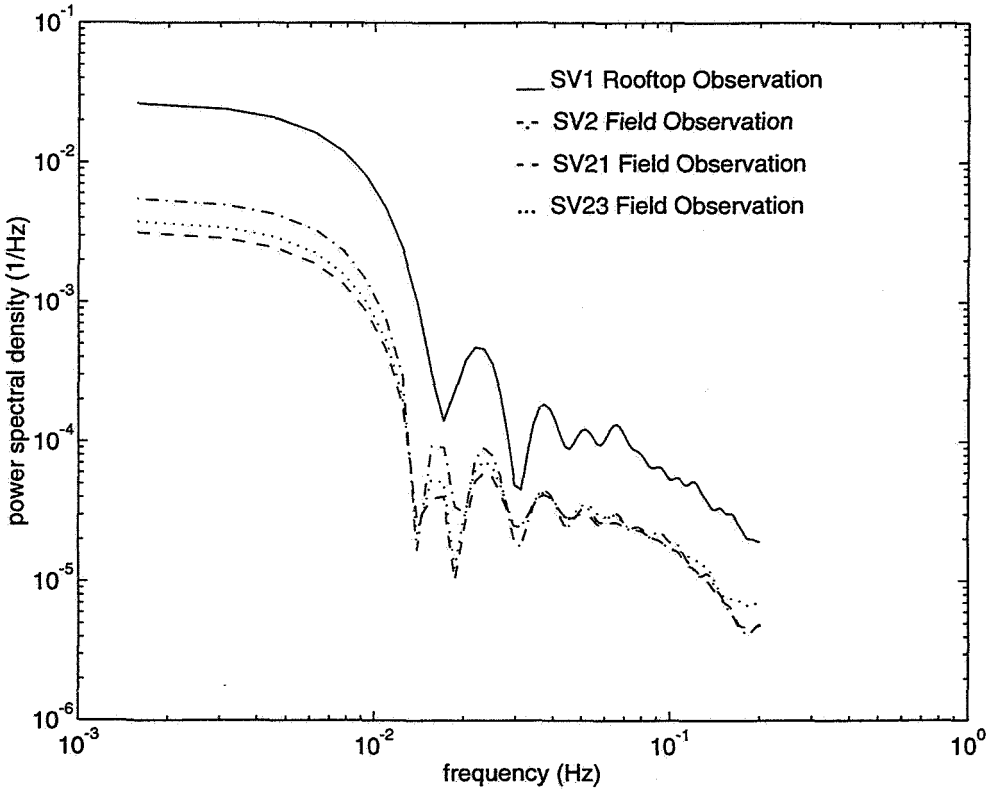

Figure 17: Comparison of Rooftop and Field Power Spectral Densities

representative spectrum obtained from the rooftop data for Baseline 1 is plotted along with the spectra for three different SV's observed in the field. In each case, the same mAster-slave antenna pair is used even though the baseline vectors differ. The large peak in SV1 at about 0.02 Hz mAy be caused by a certain rooftop multipath reflector not present in the field.

The similarities between the rooftop and field data are just as apparent when the variances of the sample data are tabulated, as in Table 2. The ratio of the variance of each of the field data series to the variance of the rooftop data is shown in the second row. The ratio of the power in the spectra for the field residuals to that of the rooftop data is nearly constant throughout the frequency range. The value of the DC power is shown in the third row of the table. From the table we see that these ratios are approximately the same as the ratios of the variances. This simple relationship allowed a straight-forward adaptation of the noise model obtained for the rooftop data to the field data. The only change necessary was to scale the input white noise by the new variance for the field data. For the rooftop data, the variance used for the entire data set was 2.4×10^{-5}. Using an approximation suggested by the ratios in the table, this variance is divided by 5 to get approximately 5×10^{-6}.

The result of the noise model adaptation to one field data set is shown in Figure 19. The simulated differential phase is the lowest of the four data signals. Again, for clarity the observations for antennas 1, 2, and 3 have been offset by 0.1, 0.2, and 0.3 cycles, respectively. The simulated signal is a compromise between simulating the low variance after 21 hours and simulating the higher variance before this time. The apparent

Variance of SV1 Rooftop Residual DAta=4.3×10^{-4}	SV2 Field	SV21 Field	SV23 Field
Variance of Field Residual DAta	8.6×10^{-5}	5.2×10^{-5}	6.2×10^{-5}
Ratio of Rooftop to Field Variance	5.0	8.3	7.0
Ratio of Rooftop to Field DC Value in PSD	4.8	8.4	7.0

Table 2: Ratios of Variance and DC Values Between Rooftop and Field DAta

correlations between antennas 1 and 2 were not modeled because the data was concatenated into one series. The corresponding power spectral densities are presented in Figure 18. The agreement in the frequency domain is quite good, having only one discrepancy at 0.02 Hz. Here the simulation follows the spectrum of antenna 3, which contains less power than those of antennas 1 and 2. The results obtained for other SV data sets are similar.

As a result of the slight adaptation of the rooftop noise model to fit the field data, two noise models are available for use in GPS differential phase simulations. In multipath-rich environments, the rooftop noise model would be recommended. The higher noise levels provide a conservative estimate of errors that might be encountered. The lower variance of the field model may represent cases where receiver antennas are not as susceptible to multipath interference. The TRACE simulation in this investigation will make use of the low-variance field model.

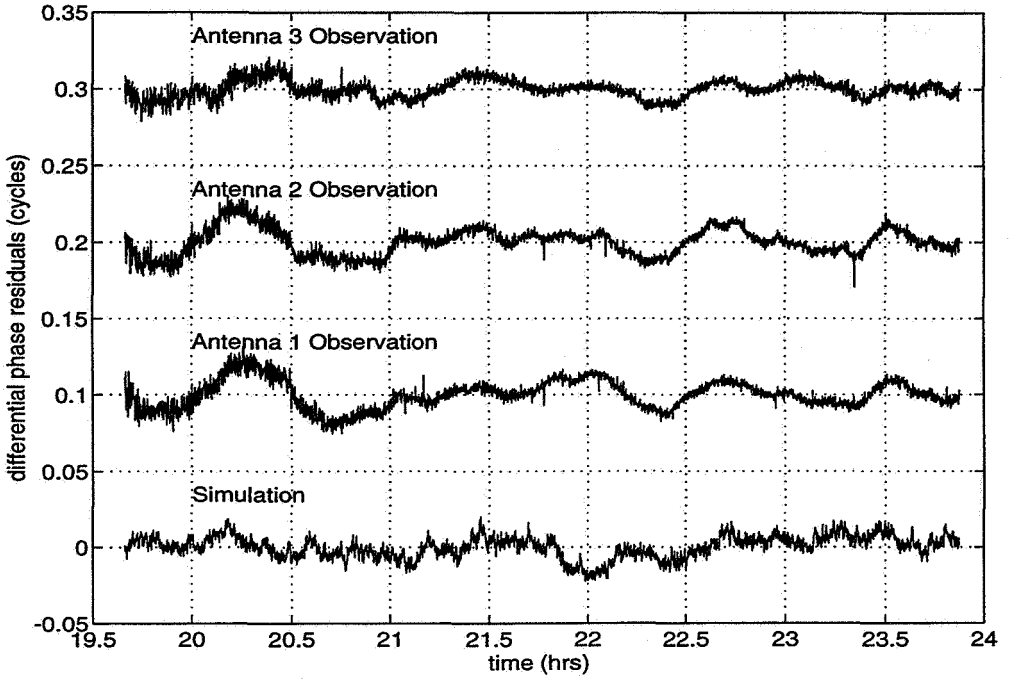

Figure 18: Field Data SV2 Observed and Simulated Differential Phase Residuals

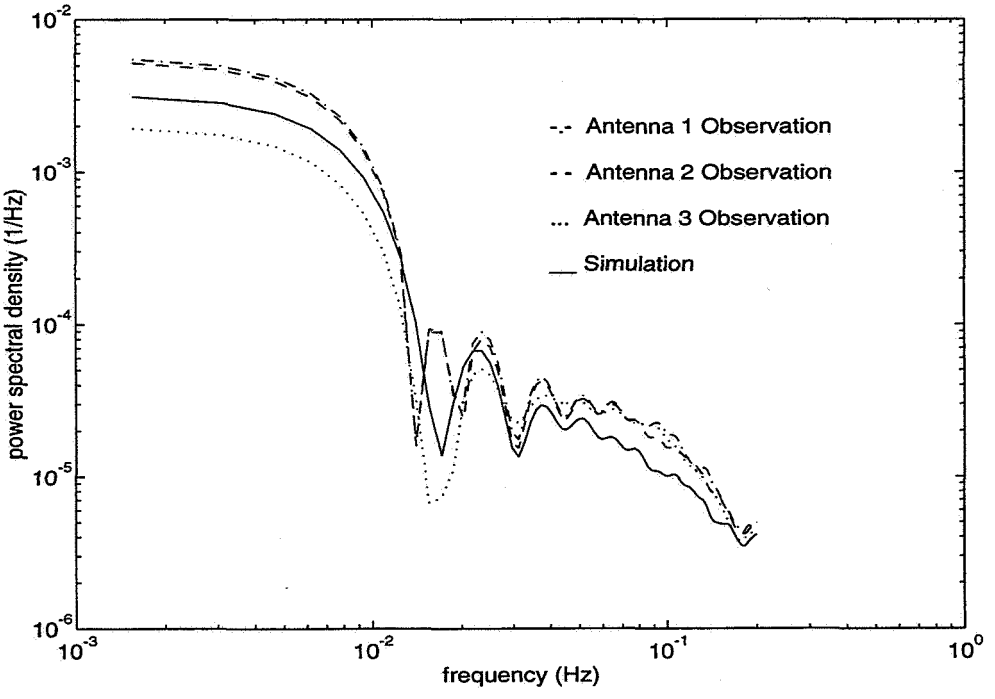

Figure 19: Field Data SV2 Observed and Simulated Power Spectral Densities

4. TRACE Measurement Simulation

In the absence of real TRACE GPS data, a simulation is required to test the effects of different antenna configurations and spacecraft attitude changes on the Kalman filter. This chapter presents the development of the simulation model.

4.1 Attitude and Position Requirements

In any GPS simulation, the constellation of the GPS SV's must be modeled. For this study, gravitational disturbing effects such as J_2 are ignored, and so the classical six orbital elements for each SV are used for the simulation.

The orbital elements of the TRACE spacecraft are also required. Because TRACE must be sun-pointing, the spacecraft will be placed into a 6am-6pm sun-synchronous orbit at an altitude of 700 km. The right ascension of the ascending node depends upon the time of year--June 21 is chosen as the epoch in this study so that the right ascension is zero. The inclination of the orbit is 98°, and the eccentricity is chosen as 1×10^{-3}.

The nominal attitude of the TRACE spacecraft is as shown in Figure 20. The positive y axis of TRACE is down the boresight of the telescope and points in the direction of the sun. Roll angles are about this axis. The northward normal to the ecliptic plane is the nominal direction of the positive z axis. Rotations about this axis are defined as yaw. The x axis, which is the pitch axis, completes the orthogonal triad.

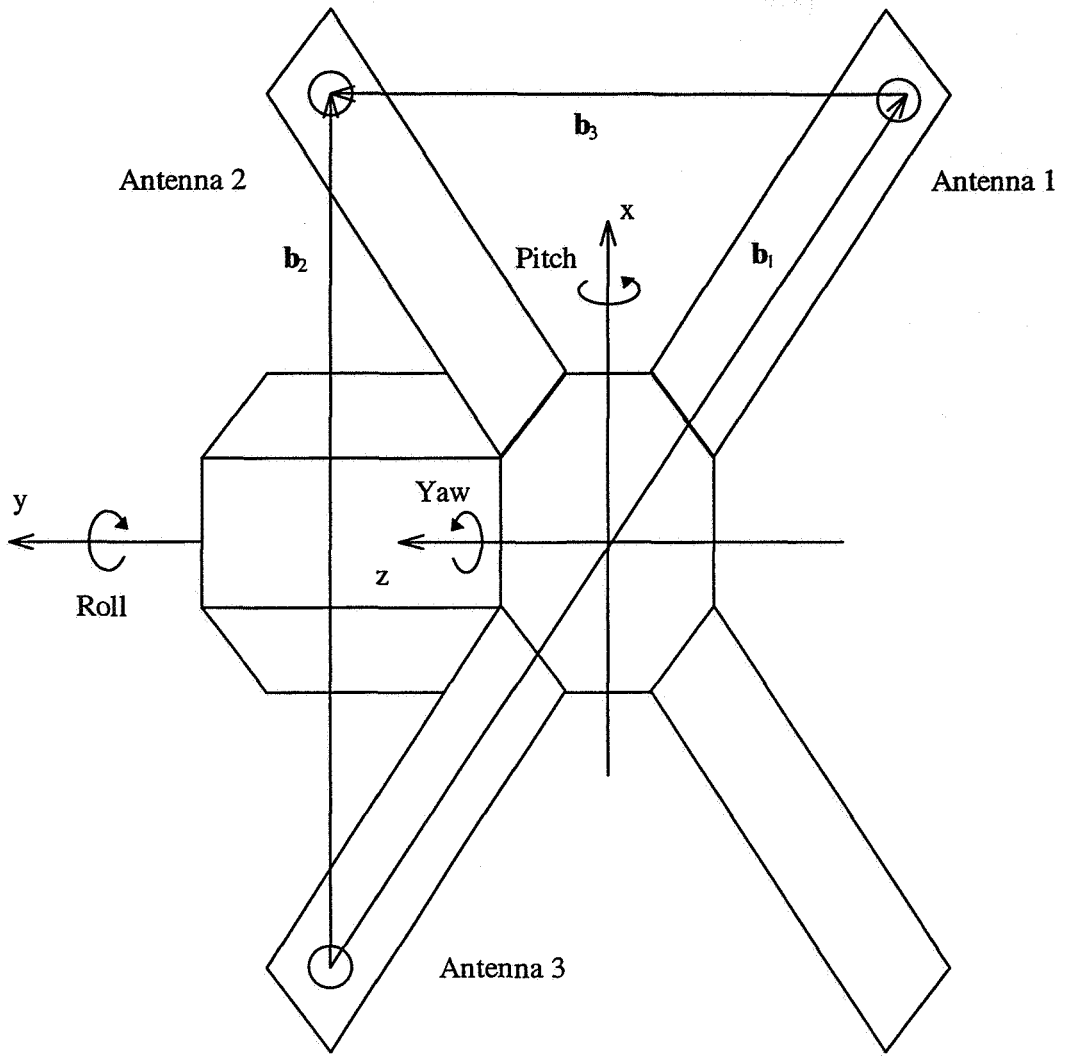

Figure 20: TRACE Spacecraft Showing GPS Antenna Configuration

The attitude control system of TRACE will be required to hold sun lock to within half a degree. Perturbations about the nominal sun-pointing orientation are thus assumed to be within a half degree also. Because the spacecraft is sun-pointing, the nominal attitude in inertial space will be nearly constant over the course of a few minutes, the duration of the simulations. Only a one degree per day drift will occur in the yaw angle due to the revolution of the earth about the sun.

4.2 Sources of Error

Before creating the simulation for TRACE simulation, the possible sources of error are determined so that they may be included in the model. The most obvious source of error is the focus of this investigation: incomplete antenna deployment. As shown in Figure 20, the antennas are to be mounted on the back of the solar panels. The panels have a single hinge at their contact point with the spacecraft body. At launch the panels will be flush with the body chassis, but will be deployed once TRACE is injected into its proper orbit. Assuming the panels deploy properly, they will form an angle of 90° with the body. The panel will be considered rigid enough that no "flapping" will occur.

In addition to the positioning error caused by the mounting structure, the antennas themselves introduce another source of error. The phase centers of the GPS are not fixed. Rather, they depend on the incident angle of the signal being collected. The baselines are therefore subject to some drift from one SV to another. The nominal position of the antenna phase centers is naturally in the physical center of the antenna, but the actual position may vary by up to one centimeter for a typical 5 cm diameter GPS antenna[20].

For the TRACE spacecraft, multipath is not expected to be a large problem. Since the antennas are on the back of the solar panels, they face away from the body of the spacecraft. This gives an unobstructed view of the GPS constellation with no nearby reflecting surfaces. Therefore, the differential phase error model with the corrections made for the field data will be used. With the noise model, some of the small unforeseen multipath effects in the TRACE experiment may be modeled.

Although the spacecraft will nominally be sun-pointing, the attitude control system (ACS) will not be able to maintain perfect pointing accuracy. Therefore, the actual attitude of the spacecraft will exhibit some oscillations as the ACS attempts to correct any errors. The angular rates will assumed small but generally nonzero.

4.3 Simulation Development

The previous analysis of the assumptions and possible sources of error in the TRACE mission has presented the parameters necessary for a realistic simulation. The error sources for the baselines are used to create a possible antenna configuration aboard TRACE. The antenna positions, orbital elements of TRACE and the SV's, and the attitude of TRACE are all then used to determine which SV's will be observed over some time period of interest. Knowing the direction of the SV's in view then allows one to form the differential phase measurements that will serve as the primary observable in the attitude determination. The procedure is described more fully below.

4.3.1 Unit Vectors to GPS Space Vehicles

The orbit of the spacecraft is first simulated. A standard algorithm is employed to convert the orbital elements of the TRACE spacecraft into inertial coordinates for the time period of interest. In the same manner, the orbital elements of all 24 satellites in the GPS constellation are used to find the positions of the SV's throughout the time span. With this information and the use of Equation 3, the unit vectors to all of the SV's are determined in the inertial frame.

4.3.2 TRACE Attitude History

The attitude of TRACE is represented by a 1-2-3 (pitch-roll-yaw) Euler angle set. For the purposes of calculating the changes in the attitude over time, however, quaternions are used. To model the attitude motion in the simplest possible way, small oscillations about the nominal pitch, roll, and yaw angles are chosen as sinusoidal functions of time. The angular rates and initial angular offsets are arbitrarily chosen for each simulation.

4.3.3 Independent Antenna Coordinate Systems

The positions of the three antennas on TRACE are required in the simulation process. Although these positions could be specified directly in the body coordinate system (BCS), another system is chosen to accentuate the role of the solar panel flap angles in the attitude determination problem. A separate coordinate system is chosen for each of the antennas. Thus three sets of 2-3-1 Euler angles are used to describe the orientation of each of the three antenna systems with respect to the BCS. The first angle ψ is a rotation about the y axis of the spacecraft designed to align the antenna x' axis with the centerline of the solar panel (See Figure 21). The second rotation α is about the antenna z' axis and is the flap angle of the solar panel about the hinge. A flap angle of zero signifies that the panel is fully deployed to its nominal position at a right angle to the y axis of the BCS. A flap angle of 90° would thus indicate that the panel did not deploy at all. Negative flap angles are possible and could indicate such an effect as solar pressure. The third rotation angle ϕ is about the x' axis and could be used to simulate a twisting of the solar panel. In Figure 21, the antenna is positioned on the back of the solar panel and faces away from the sun at full deployment.

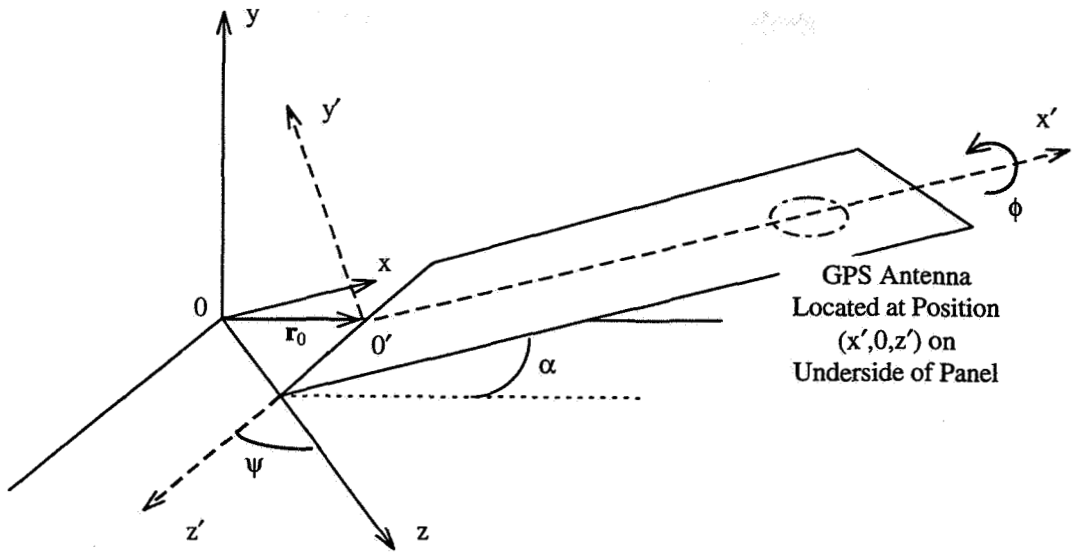

Figure 21: Solar Panel Coordinate System

The flap angle is the only one of the three Euler angles used in the antenna coordinate systems that will vary in the simulations. The flap angles for antennas 1, 2, and 3 will be referred to as α_1, α_2, and α_3, respectively. The set of 2-3-1 Euler angles used for each of the three antenna systems are shown in Table 3. These angles are used to form a transformation matrix from the BCS to each of the antenna coordinate systems. The transformation matrices are labeled ${}^{A1}\mathbf{C}^{B}$, ${}^{A2}\mathbf{C}^{B}$, and ${}^{A3}\mathbf{C}^{B}$ for antennas 1, 2, and 3, respectively. The form of the transformation matrix for a 2-3-1 set of Euler angles is

$$ {}^{A}C^{B} = \begin{bmatrix} \cos\alpha\cos\psi & \sin\alpha & -\cos\alpha\sin\psi \\ -\sin\alpha\cos\psi & \cos\alpha & \sin\alpha\sin\psi \\ \sin\psi & 0 & \cos\psi \end{bmatrix} \qquad (43) $$

where the fact that the third Euler angle ϕ equals zero has already been taken into account.

The reason for choosing these antenna-specific coordinate systems is that the main sources of antenna position errors are isolated. The antenna phase centers are not

	Antenna 1	Antenna 2	Antenna 3
1st Rotation ψ	-45°	45°	135°
2nd Rotation α	α_1	α_2	α_3
3rd Rotation ϕ	0°	0°	0°

Table 3: Euler Angles of Antenna Coordinate Systems with Respect to Body Frame

expected to differ by more than a centimeter from the nominal positions on the solar panel. However, a flap angle greater than 60° for antenna 1 would change the apparent x position of Baseline 1 by 27 cm in the body coordinate system, a change greater than the L1 wavelength. In the coordinate system of the antenna, the x' position is still less than a centimeter. Only the flap angle deviates from its nominal position. Isolating the sources of error generally improved the ability to solve for them independently.

4.3.4 Use of Antenna Positions to Determine Baselines

The next step in the formation of the differential phase data is to determine the baselines in the body frame. The transpose of the transformation matrices introduced above are used to convert the locations of the antennas in the antenna coordinate systems into coordinates in the BCS. The origins of the antenna frames must also be considered to properly locate the antennas in the body frame. The vector $\mathbf{r}_0$ from the BCS origin to the antenna frame origin is indicated in Figure 21. The location of antenna 1, for example, in the body frame is given by

	Antenna 1 (m)	Antenna 2 (m)	Antenna 3 (m)
x_0	0.356	0.356	-0.356
y_0	0	0	0
z_0	-0.356	0.356	0.356

Table 4: Origins of Antenna Coordinate Systems in Body Frame

	Antenna 1 (m)	Antenna 2 (m)	Antenna 3 (m)
x'	0.736	0.736	0.736
y'	0	0	0
z'	0	0	0

Table 5: Nominal Antenna Positions in Antenna Reference Frames

$$\mathbf{r}_1 = \mathbf{r}_{01} + {}^{B}\mathbf{C}^{A1}\mathbf{r}_1^{A1} \tag{44}$$

where $\mathbf{r}_1^{A1}$ is the position vector of antenna 1 in the antenna 1 reference frame and $\mathbf{r}_{01}$ is the position vector of the corresponding origin. The locations of the antenna frame origins in the BCS are given in Table 4, and the nominal positions of the antennas in the individual antenna frames are given in Table 5. In the nominal positions, the antenna phase centers lie along the centerline of the solar panel and directly on the surface. The only nonzero component is in the x direction out along the panel and is the same for all three antennas.

With knowledge of the antennas in the body frame, the baselines may be formed by differencing the antenna position vectors. The baselines will be defined as:

$$\begin{aligned} \mathbf{b}_1 &= \mathbf{r}_1 - \mathbf{r}_3 \\ \mathbf{b}_2 &= \mathbf{r}_2 - \mathbf{r}_3 \\ \mathbf{b}_3 &= \mathbf{r}_2 - \mathbf{r}_1 \end{aligned} \tag{45}$$

Several other combinations of differences may be formed, but only two baselines are independent. In the above arrangement, antenna 3 serves as the master for baselines 1 and 2. Only two of the three baselines are independent, for the remaining baseline is simply the difference of the other two: $\mathbf{b}_3=\mathbf{b}_2-\mathbf{b}_1$.

4.3.5 Determination of Observable GPS Space Vehicles

Another step in the creation of the simulated differential phase data is to determine which SV's are observed by each of the antennas. Based on the position of the TRACE spacecraft and the positions of the SV's, one can determine which SV's are obscured by the Earth[21]. The attitude of TRACE and of the individual solar panels are then used to select from the remaining SV's those that are in view of all three antennas simultaneously.

The unit vectors to the SV's are first transformed into each of the antenna frames. For example, the unit vector to the j^{th} SV in the antenna 2 reference frame is

$$\tilde{\mathbf{e}}_j^{A2} = {}^{A2}\mathbf{C}^{B}\,{}^{B}\mathbf{C}^{I}\,\tilde{\mathbf{e}}_j^{I} \tag{46}$$

where ${}^{B}\mathbf{C}^{I}$ is the inertial to body transformation matrix obtained from the attitude of TRACE. Referring again to Figure 21, the boresight of the antenna is in the $-y'$ direction of its coordinate system. Thus the negative normal $-\mathbf{n}=[0\ -1\ 0]^T$ to the plane of the solar panel is used as the boresight vector. The elevation angle of the j^{th} SV can then be determined from

$$elevation_j = \frac{\pi}{2} - \cos^{-1}\left(-\mathbf{n}\cdot\tilde{\mathbf{e}}_j^{A2}\right). \tag{47}$$

If this elevation angle is less than 5°, the GPS satellite is considered out of view by antenna 2. This process is repeated for each of the antennas and for each satellite not obscured by the Earth.

It is assumed that the GPS receiver aboard TRACE will only lock onto those SV's observed by all three antennas simultaneously. This further limits the number of SV's which are available for attitude determination. Simulations run with all three solar panels in nominal positions indicate that 5-6 SV's are usually observable. The total number is limited to six because the receiver is assumed to have only six channels per antenna for SV tracking. Thus, although up to 12 SV's may be in view at a time, no more than six SV's are tracked. The data is formatted by selecting six differential phase measurements, if possible, at a time from the available set. If six SV's are not in view, some of the channels will report no phase data. Furthermore, each channel maintains lock on one particular SV until it goes out of view. Data from another SV not currently tracked by the other five channels is then immediately put on this channel. (Data drop-outs are not simulated.)

4.3.6 Formation of Differential Phase Data

The final stage in the formation of the simulated data is to use Equation 7 for the differential phase, which was derived in Section 2.1.2, Differential Phase Equations:

$$\Delta\varphi_{ij} = \frac{\mathbf{b}_i \cdot \tilde{\mathbf{e}}_j}{\lambda} - k_{ij} + \beta_i + \mu_{ij} \qquad (48)$$

where both vectors are expressed in the body frame. The integer phase count k_{ij} is determined by

$$k_{ij} = \text{floor}\left(\frac{\mathbf{b}_i \cdot \tilde{\mathbf{e}}_j}{\lambda}\right) \tag{49}$$

Here, the unit vector is taken when the satellite is first observed and the function *floor* rounds the operand to the nearest integer toward negative infinity. Since the integer is only determined when the SV is first sighted, the differential phase will begin in the range (-1,1) but may be well outside this range by the time the SV goes out of sight. This is done to simplify the calculations.

The remaining quantity μ_{ij} in Equation 49 is the noise determined from the model of Section 3, Noise Model Development. The model obtained for the JSC field data is used because the low multipath environment of the field matches the conditions aboard TRACE better than the rooftop environment. Since the noise model was developed for a data collected at a sampling rate of once every 2.5 seconds, the same frequency is used for the TRACE simulation. The final result of the simulation is a history of differential phase measurements for all observable GPS SV's over the time interval specified.

5. TRACE Attitude Determination

The attitude determination algorithms developed here are based on the preliminary TRACE Attitude Control System software provided by NASA Goddard Space Flight Center. For the TRACE spacecraft, measurements from sun sensors and magnetometers are Kalman filtered to provide the attitude information necessary for the science mission. The system is fully functional without the use of GPS measurements. However, a GPS receiver and antennas are to be included as a test of GPS attitude determination capabilities. This chapter describes the methods used to create this set of algorithms, which are designed to be consistent with the methodologies presented in the ACS software document. The algorithms have the same structure as the magnetometer and sun sensor attitude update modules. The GPS code is in fact designed to be merged with the existing code and even to replace the magnetometer and sun sensor modules if desired.

5.1 Baseline-Attitude Ambiguity

Before utilizing a Kalman filter for attitude determination, the baselines must be well-known. For attitude accuracy of 0.5 degrees with a 2 meter baseline, errors in antenna position cannot exceed (2 m)sin(1/2)=2 cm. The problem inherent in the use of deployable-mounted antennas for GPS attitude determination aboard TRACE is that knowledge of the baselines may not meet this requirement. Undeployed solar panels could possibly affect the positions of the antennas in the body frame. Therefore, the baselines must either be included in the state to be determined in the Kalman filter or be calculated before the filtering process begins.

In addition to the positions of the antennas, the line biases and integer ambiguities are required for accurate attitude knowledge. Unfortunately, not all of these quantities are independent. The flap angles of the solar panels directly affect the apparent attitude of the plane formed by the two baselines. An error in the x' location of the antennas on the solar panels may appear as part of the line biases. Likewise, an error in the z' position may look like a roll angle error. Furthermore, an approximate attitude is required to resolve the integer ambiguities. As a result, it is not possible to solve for all of these quantities at once. Some assumptions are necessary to begin the process of attitude determination.

5.2 Two-Step Solution Process

In order to overcome the difficulties in determining the baselines and the attitude of the spacecraft accurately, a two-step process, which requires some assumptions, will be employed. First, the baselines are determined in the inertial frame. This process is begun by assuming the spacecraft has a nominal attitude and that the solar panels are all fully deployed. Thus, the baselines are assumed to be nominal as well. A batch filter is then used to solve for changes in the baselines and the integer ambiguities. These changes are then converted to the body frame and added to the nominal baseline, resulting in a set of observed baselines in the body frame. The angle between the nominal and observed baselines in the nominal x-z plane of the solar panels is assumed to be the roll angle. This roll angle is used to rotate the observed baselines into the new estimate of the body frame. The flap angles are then determined geometrically from the equations defining the baselines.

Using a Kalman filter to solve for the attitude is the second step in the attitude determination process. This stage uses the baselines and roll angle resulting from the batch filter initialization to refine the estimates of the pitch, roll, and yaw sequentially.

5.2.1 Least-Squares Baseline Determination

The methods described in this section are based largely on the work of Axelrad *et al*[22]. Here, however, initial attitude assumptions will be used to determine whether the actual baselines differ largely from their nominal values. The baseline errors for TRACE could be more than the L1 carrier wavelength. In order to begin the process of determining the baselines, it is assumed that TRACE is pointing at the sun with a pointing error less than 0.5°. Thus, the initial errors of the pitch and yaw angles are bounded. Although the spacecraft may be at any roll angle, the first estimate is that the roll is nominal.

Some further assumptions are necessary to begin the batch filter process. A least-squares filter will be used as it was in the development of the noise model. As before, the filter is used to solve for corrections to the baseline vectors. (Here, the inertial frame is used rather than the ECEF frame.) Thus, an initial estimate of the baselines must be made. It is natural to assume the baselines are nominal in the body frame. The body frame baselines are then converted to the inertial frame using the initial estimate of the transformation matrix to write $\mathbf{b}_i^I = {}^I\mathbf{C}^B\mathbf{b}_i^B$. What differs from the previous least-squares developments is that the lengths of the baseline correction vectors in the inertial frame are not limited to less than one L1 wavelength, or 19 cm. Suppose, for example, that the antennas are in their correct positions in the body frame but that the roll angle is 180° away from nominal. The apparent baseline vector in inertial space will be rotated 180° as

well. The length of the vector difference is therefore twice the length of the baseline: 4 meters for a 2 meter baseline.

The fact that the baselines are free to vary by such a large amount makes it necessary to solve for the integer ambiguities in the batch filter, as well. Furthermore, the line biases must be taken into account. The differential phase in Equation 7 may be written in another form to make this process easier:

$$\begin{aligned} \Delta\varphi_{ij} &= \frac{\mathbf{b}_i \cdot \tilde{\mathbf{e}}_j}{\lambda} - k_{ij} + \beta_i + \mu_{ij} \\ &= \frac{\mathbf{b}_i \cdot \tilde{\mathbf{e}}_j}{\lambda} - K_{ij} + \mu_{ij} \end{aligned} \tag{50}$$

where

$$K_{ij} = k_{ij} - \beta_i \tag{51}$$

The quantity K_{ij} is a real number and must be determined for each SV-baseline pair. Following the development of the least-squares solution in Section 3.2, Residual Formation, a state vector $\mathbf{x}$ is formed. For one baseline, the line bias term β in Equation 24 is replaced with six K_j's corresponding to six different SV's.

$$\mathbf{x} = \begin{bmatrix} \delta b_x \\ \delta b_y \\ \delta b_z \\ K_1 \\ K_2 \\ \vdots \\ K_6 \end{bmatrix} \tag{52}$$

The full matrix equation for this state is similar to Equation 27 and is given by

$$\begin{bmatrix} \delta\Delta\varphi_1(t_1) \\ \delta\Delta\varphi_2(t_1) \\ \vdots \\ \delta\Delta\varphi_6(t_1) \\ \hline \delta\Delta\varphi_1(t_2) \\ \delta\Delta\varphi_2(t_2) \\ \vdots \end{bmatrix} = \begin{bmatrix} \mathbf{H}_1(t_1) \\ \mathbf{H}_2(t_1) \\ \vdots \\ \mathbf{H}_6(t_1) \\ \hline \mathbf{H}_1(t_2) \\ \mathbf{H}_2(t_2) \\ \vdots \end{bmatrix} \mathbf{x}$$

$$= \begin{bmatrix} e_{1x}(t_1) & e_{1y}(t_1) & e_{1z}(t_1) & -1 & 0 & \cdots & 0 \\ e_{2x}(t_1) & e_{2y}(t_1) & e_{2z}(t_1) & 0 & -1 & & \\ & & & \vdots & & \ddots & \\ & & & 0 & & & -1 \\ e_{1x}(t_2) & e_{1y}(t_2) & e_{1z}(t_2) & -1 & 0 & \cdots & 0 \\ e_{2x}(t_2) & e_{2y}(t_1) & e_{2z}(t_2) & 0 & -1 & & \\ & & & \vdots & & \ddots & \end{bmatrix} \mathbf{x} \qquad (53)$$

Slight differences in the format of the data have been made from Equation 27, but the forms are similar. More importantly, the least-squares solution is found in exactly the same way as before. The pseudo-inverse of the observation matrix given is used to solve for the state **x** as described by Equation 29.

The method of least-squares has resulted in baseline correction vectors and a set of parameters K_j for each baseline. Taking advantage of the fact that the k_j's are integers, one may simply round the parameters K_j to find that k_j=int(Kj). Since the line bias is constant over short periods of time and is assumed to lie in the range (-1,1), it may be found by using Equation 51 to write

$$\beta = \overline{(k_j - K_j)} = \overline{\{\text{int}(K_j) - K_j\}} \qquad (54)$$

where the average is taken over the six K_j's.

The baselines corrections found in the least-squares solution are added to the nominal baselines to form the observed baselines in the body frame. The transformation matrix from the inertial to body frame ${}^{B}\mathbf{C}^{I}$, assuming a nominal attitude, is used to make the conversion. The best estimate of the baselines is thus given by

$$\hat{\mathbf{b}}_i^B = \mathbf{b}_i^B + {}^{B}\mathbf{C}^{I}\delta\mathbf{b}_i^I \tag{55}$$

The observed baselines $\mathbf{b}_1$ and $\mathbf{b}_2$ are then used to estimate the roll angle of the TRACE spacecraft.

5.2.1.1 Roll Angle

To estimate the roll angle of TRACE, Baseline 1 in Figure 20 is used. Because this baseline passes through the axis of symmetry of the spacecraft, the components of this baseline in the x-z plane of the body frame are not affected by changes in the flap angles. For example, even if flap angle α_1 is 90°, the projection of the observed baseline vector onto the x-z-plane of the body frame is still parallel to the nominal baseline. The angle between this projected vector and the nominal baseline vector is thus assumed to be the roll angle.

The process is begun by expressing the observed baseline 1 in the body frame with the assumption that the pitch, roll, and yaw angles are all nominal. If Baseline 1 was also nominal, the angle formed by the x-z components of the baseline would be 45°. The roll angle is just the difference between the angle formed by the observed baseline and 45°. The knowledge of the roll angle is then used to update the transformation matrix from the

inertial to body frame. With this correction, the observed baselines are rotated into the new estimate of the body frame.

5.2.1.2 Deployment Angle Errors

In order to determine the attitude of TRACE, the baselines must be fully defined in the body frame. This requires that the flap angles, or deployment angle errors, of the solar panels be known since the angles directly affect the apparent pitch and yaw of the spacecraft. The geometry of the three antennas used to form the two baselines is used to solve for a set of possible flap angles.

The baselines in the body frame are written as function of the flap angles by using the definitions of the baselines and the positions of the antennas as given in Equations 45 and 44, respectively. The equation for baseline 1 is

$$\begin{aligned}\mathbf{b}_1 &= \mathbf{r}_1 - \mathbf{r}_3 \\ &= \mathbf{r}_{01} + {}^{B}\mathbf{C}^{A1}\mathbf{r}_1^{A1} - \mathbf{r}_{03} - {}^{B}\mathbf{C}^{A3}\mathbf{r}_3^{A3} \\ &\equiv \Delta\mathbf{r}_{01} + \left({}^{A1}\mathbf{C}^{B}\right)^{\mathrm{T}}\mathbf{r}_1^{A1} - \left({}^{A3}\mathbf{C}^{B}\right)^{\mathrm{T}}\mathbf{r}_3^{A3}\end{aligned} \qquad (56)$$

where $\Delta\mathbf{r}_0$ is the difference in the positions of the origins and $\mathbf{b}_1$ is the observed baseline resulting from the least-square batch process. It is assumed that the antennas are in their nominal positions so that only the x' components of $\mathbf{r}_1^{A1}$ and $\mathbf{r}_2^{A2}$ are nonzero. This component will be referred to simply as x' since it is equal for each antenna. Substituting the transpose of Equation 43 into Equation 56 results in

$$\mathbf{b}_1 = \Delta\mathbf{r}_{01} + \begin{bmatrix} \cos\alpha_1\cos\psi_1 & -\sin\alpha_1\cos\psi_1 & \sin\psi_1 \\ \sin\alpha_1 & \cos\alpha_1 & 0 \\ -\cos\alpha_1\sin\psi_1 & \sin\alpha_1\sin\psi & \cos\psi_1 \end{bmatrix} \begin{bmatrix} x' \\ 0 \\ 0 \end{bmatrix}$$
$$- \begin{bmatrix} \cos\alpha_3\cos\psi_3 & -\sin\alpha_3\cos\psi_3 & \sin\psi_3 \\ \sin\alpha_3 & \cos\alpha_3 & 0 \\ -\cos\alpha_3\sin\psi_3 & \sin\alpha_3\sin\psi_3 & \cos\psi_3 \end{bmatrix} \begin{bmatrix} x' \\ 0 \\ 0 \end{bmatrix} \qquad (57)$$
$$= \Delta\mathbf{r}_{01} + \begin{bmatrix} \cos\alpha_1\cos\psi_1 \\ \sin\alpha_1 \\ -\cos\alpha_1\sin\psi_1 \end{bmatrix} x' - \begin{bmatrix} \cos\alpha_3\cos\psi_3 \\ \sin\alpha_3 \\ -\cos\alpha_3\sin\psi_3 \end{bmatrix} x'$$

The above vector equation may be simplified significantly by applying a rotation to the observed baseline vectors. A solar panel coordinate system is chosen such that $\mathbf{b}_1$ lies along the principal direction. No other rotations are made. This single rotation about the *y*-axis of the body frame is equivalent to setting the ψ_i values in Table 3 to ψ_i-45°. By doing this, the ψ_i angles become 0°, -90°, and -180° for antennas 1, 2, and 3, respectively. The resulting equations in scalar form are

$$S_{1x} \equiv \frac{b_{1y} - \Delta r_{01x}}{x'} = \cos\alpha_1 + \cos\alpha_3 \qquad (58)$$

$$S_{1y} \equiv \frac{b_{1x} - \Delta r_{01y}}{x'} = \sin\alpha_1 - \sin\alpha_3 \qquad (59)$$

$$S_{1z} \equiv \frac{b_{1x} - \Delta r_{01z}}{x'} = 0 \qquad (60)$$

Here, the S_1 terms are the result of the least-squares solution for the observed baselines.

The development of the equations for Baseline 2 is analogous to that of Baseline 1 and provides three additional scalar equations relating α_2 and α_3 to the observations:

$$S_{2x} \equiv \frac{b_{2y} - \Delta r_{02x}}{x'} = \cos\alpha_3 \tag{61}$$

$$S_{2y} \equiv \frac{b_{2x} - \Delta r_{02y}}{x'} = \sin\alpha_2 - \sin\alpha_3 \tag{62}$$

$$S_{2z} \equiv \frac{b_{2x} - \Delta r_{02z}}{x'} = \cos\alpha_2 \tag{63}$$

Equation 60 gives no information in the form shown but is actually the result of the roll angle determination. It is included here to illustrate that the system of Equations 58-63 is an underdetermined one. The six unknowns are the sines and cosines of each of the three flap angles. The system has only five independent equations, however. The cosines of α_1 and α_3 are obtained directly from Equations 61 and 63, and the former equation is used in Equation 58 to write

$$\cos\alpha_1 = S_{1x} - \cos\alpha_3 = S_{1x} - S_{2x} \tag{64}$$

If no noise were present in the differential phase measurements, the baselines would be determined exactly from the least-squares filter. Then assuming the flap angles all lie in the range [0°,90°], the inverse cosine function could be used to find the correct flap angles. However, the presence of noise may cause some of the cosine terms to be greater than one, resulting in imaginary flap angles. The sine terms are desired because the arctangent function is defined for any real number. Hence, the ratio of the sine to cosine terms will always result in real flap angles.

Two equations, 59 and 62, and three unknowns, the sine of each angle, remain to be determined. The flap angle whose cosine term is less than one is found by using arccos.

The sines of the remaining two flap angles are then found by Equations 59 and 62 and are used together with the corresponding cosine terms to find the real-valued angles.

5.2.1.3 Results of Roll and Deployment Angle Estimation

Several test cases are used to measure the robustness of the roll and flap angle algorithms. A Monte Carlo study was done for these cases to estimate the root mean square (RMS) errors. To reduce the effects of a particular GPS constellation geometry in each case, 20 simulation runs were made for each of two orbital regions: the equator and the poles. The results from the ascending and descending nodes were combined to provide a reasonable estimate of equatorial algorithm performance, and the same was done for simulation results at the poles.

The roll angles and flap angles used in the simulations are shown in Table 6. Each case is examined up to a maximum of 8 minutes of simulation time. The simulations are performed by finding the least-squares solution for the baselines with different length data sets. The data is collected at 0.4 Hz, and the least-squares filter is applied to data with time spans of 0.5, 1, 2, 4, and 8 minutes. For all cases, the line biases are zero. In Cases 1-6, the pitch and yaw are set to zero. In Cases 7 and 8, errors are introduced by randomly choosing pitch and yaw angular errors in the range [-0.5, 0.5]. For all cases, the three Euler angles of pitch, roll, and yaw are held constant.

Case	Roll (deg)	Flap Angle 1 (deg)	Flap Angle 2 (deg)	Flap Angle 3 (deg)
1	0	0	0	0
2	60	0	0	0
3	0	90	0	0
4	0	0	90	0
5	0	0	0	10
6	0	0	10	10
7	0	0	0	0
8	0	90	0	0

Table 6: True Roll and Flap Angles for Monte Carlo Case Studies

The first case studied is the nominal Case 1, in which the roll angle and all of the flap angles are zero. The least-squares fit provides correction vectors to baselines 1 and 2. The RMS of the baseline errors for the first case are presented in Figure 22. After 8 minutes, the baselines are known to within 4 cm. The next figure, Figure 23(a), shows the maximum integer ambiguity error. It is seen here that the integers are completely determined after using 4 minutes of data. Part (b) of the same figure shows the RMS line bias errors expressed in cm. The final line bias errors for both baselines are less than 1 cm. The roll angle for Case 1 is determined by using the baseline corrections, and the resulting RMS errors are shown in Figure 24(a). After 8 minutes, the roll is known to 0.7°.

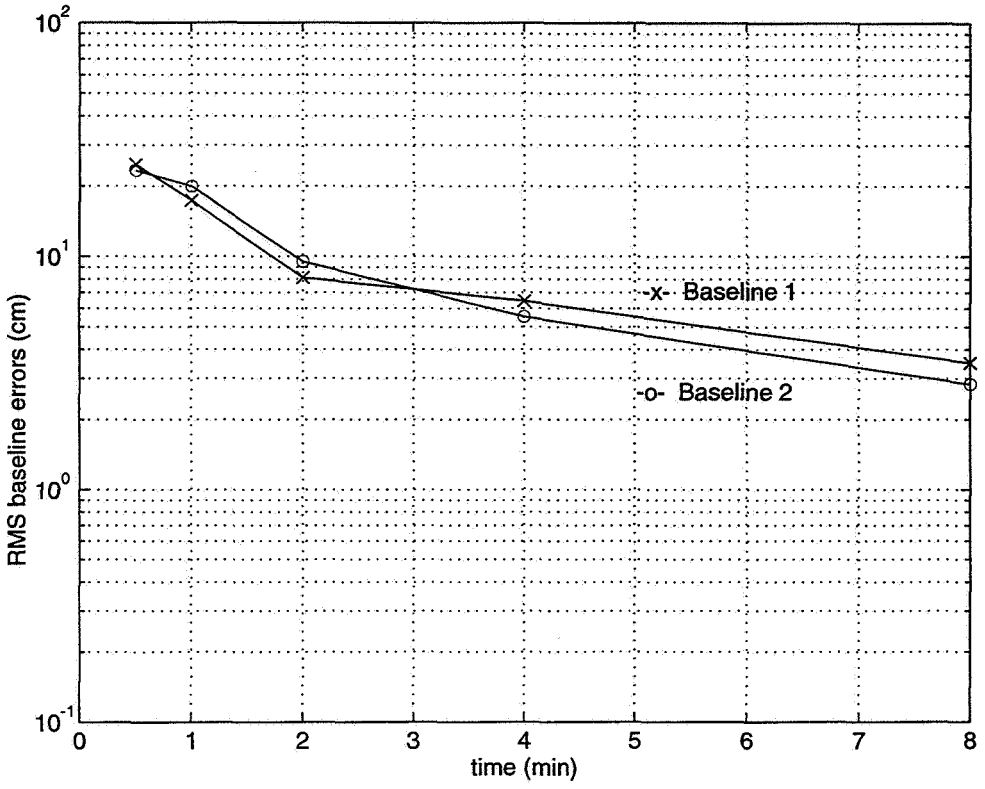

Figure 22: Case 1 RMS Baseline Errors

The fact that the flap angles are not well-determined independently is demonstrated in Figure 24(b), in which the RMS deployment angle errors are plotted. In the geometric analysis of the baselines, only the differences of the sines of the deployment angle errors were computed independently. Thus the plane formed by the two baselines is well-determined, but the distance of this plane from the origin of the spacecraft body frame is not. As a result, the differences between the flap angles in Figure 24(b) approach zero as they should for this case even though the actual deployment angle errors are large.

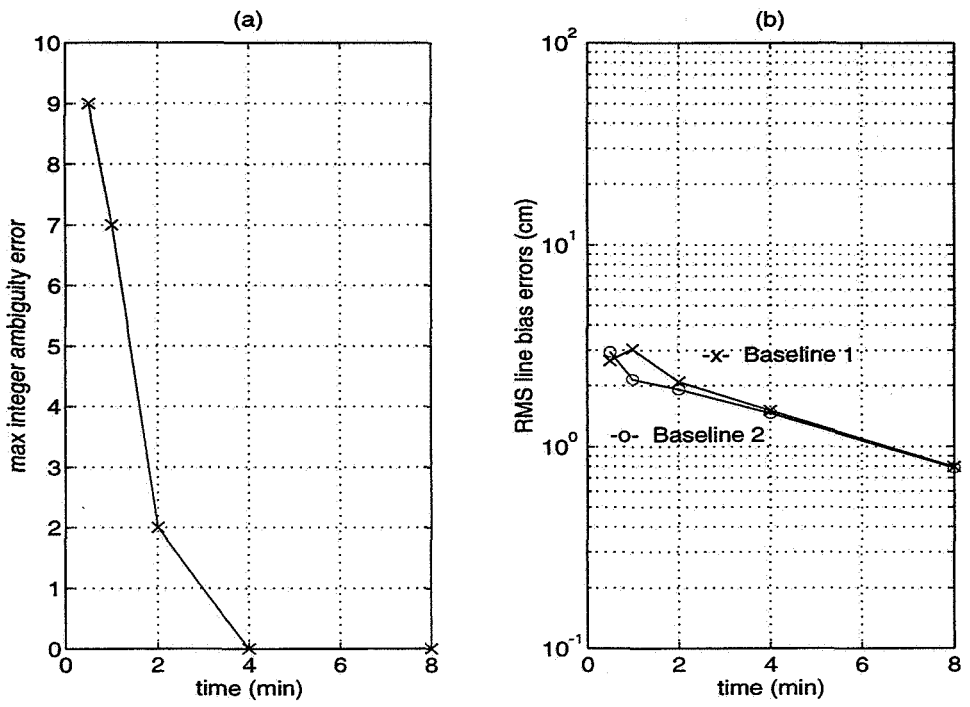

Figure 23: Case 1 Maximum Integer Ambiguity Error and RMS Line Bias Errors

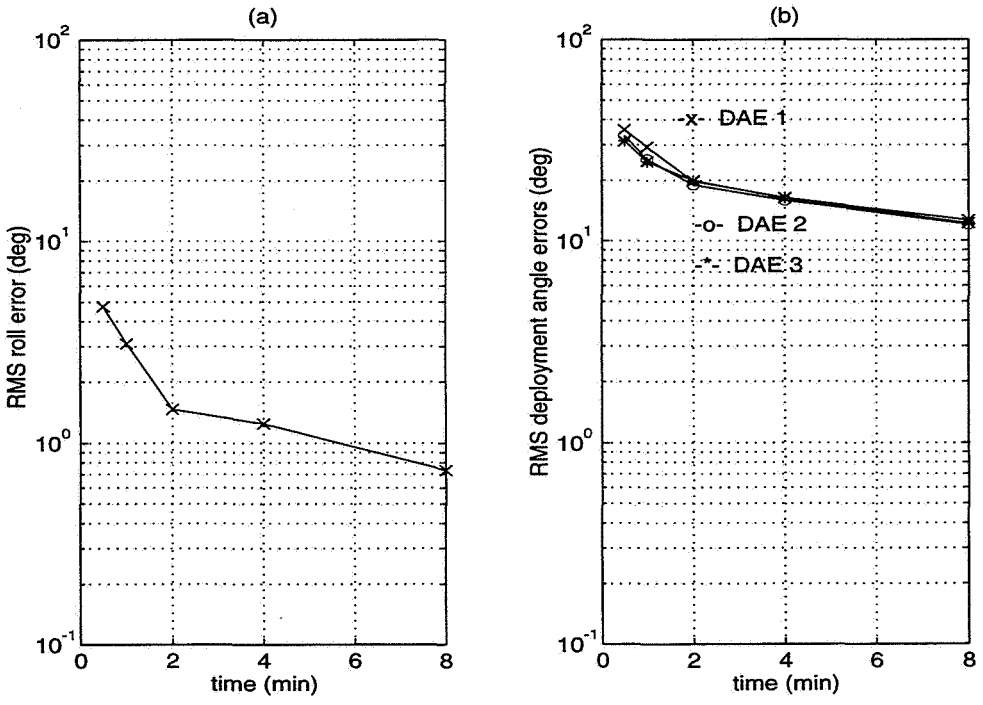

Figure 24: Case 1 Roll Angle and Deployment Angle Errors

The large deployment angle errors seen in Figure 24(b) are caused by having to calculate one angle with insufficient information, as discussed in the last section. The other two angles are calculated from this first estimate, and so any errors will be shared by all three. The correlation of these angular errors is shown in Figure 25. As seen in the figure, the errors in the angles for each trial are directly related.

To explore the correlation more fully, the eigenvalues of the covariance matrix for the deployment angles errors were calculated for each time span. The standard deviations are shown in Figure 26. Here, the large eigenvalue corresponds to the one flap angle that must be estimated with the least amount of information. The final value for this is about 20°, and the other two eigenvalues decrease to 0.9° and 0.3°. Thus, knowing one angle exactly would permit the others to be determined to less than a degree.

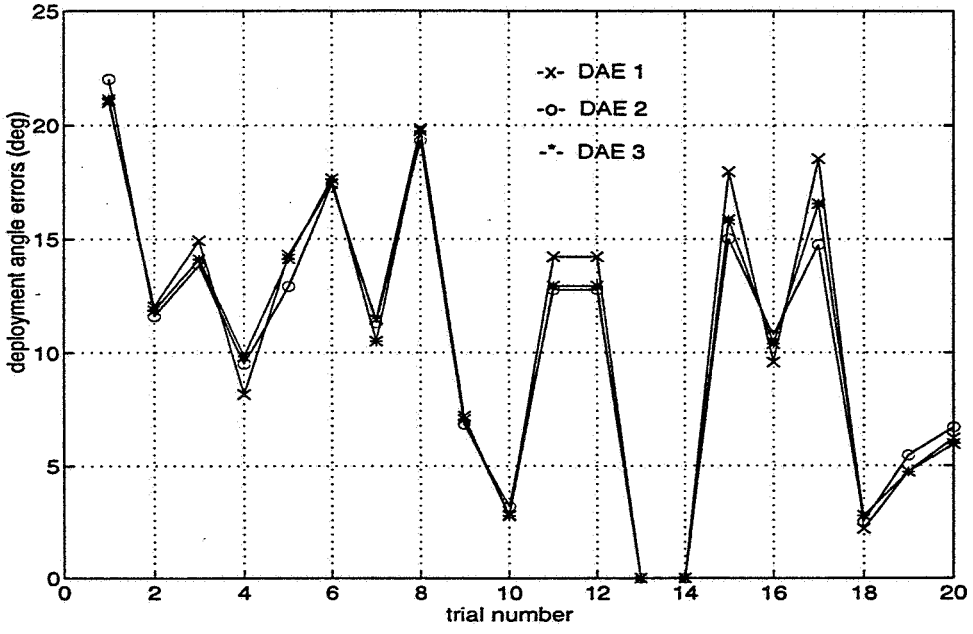

Figure 25: Case 1 Correlation of Deployment Angle Errors Across Trials

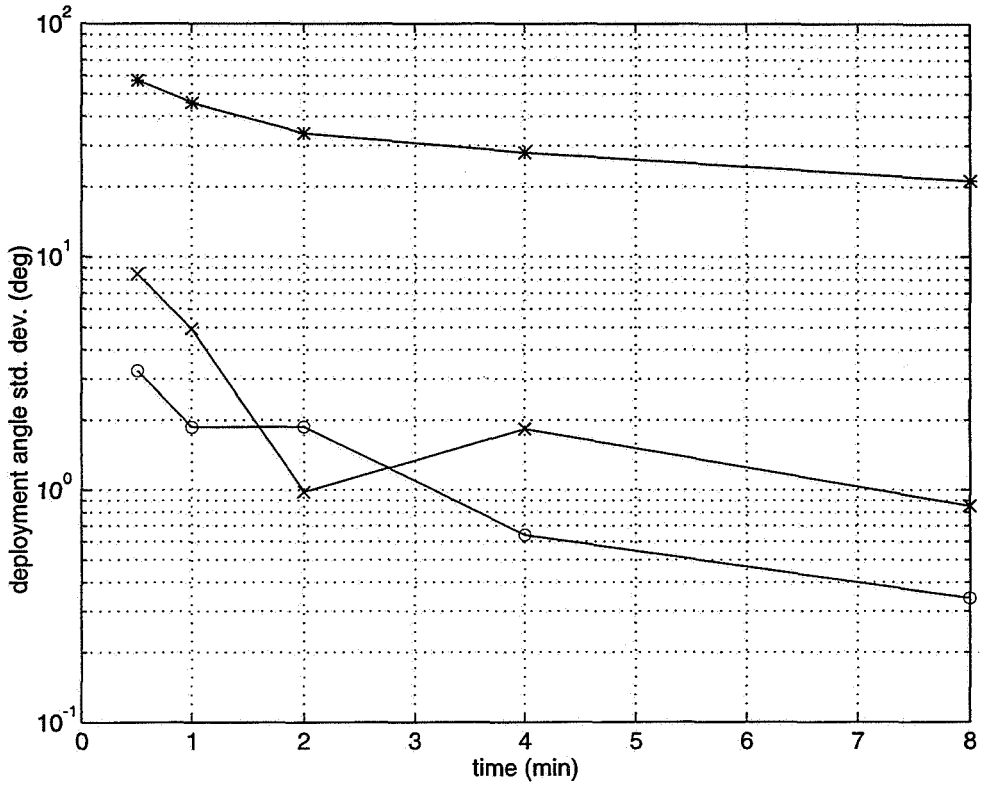

Figure 26: Case 1 Eigenvalues of Deployment Angle Covariance Matrix

The results for Case 3 of Table 6 are shown in Figure 27 through Figure 30. In the first of these, it is seen that the baselines are determined within 5 cm after 4 minutes and within 2.5 cm after 8 minutes. The integers are resolved after 4 minutes (See Figure 28(a)). Again, the deployment angle errors are not all well-determined (See Figure 29(b)). In this case, the deployment angle for antenna 1 is calculated within a degree of 90°, but the other two are found with only 5° accuracy. This is explained by the fact that angles greater than 90° were made exact in the computations. The eigenvalues of the deployment angle covariance are shown in Figure 30, which shows that only one of the three solar panel flap angles cannot be determined well.

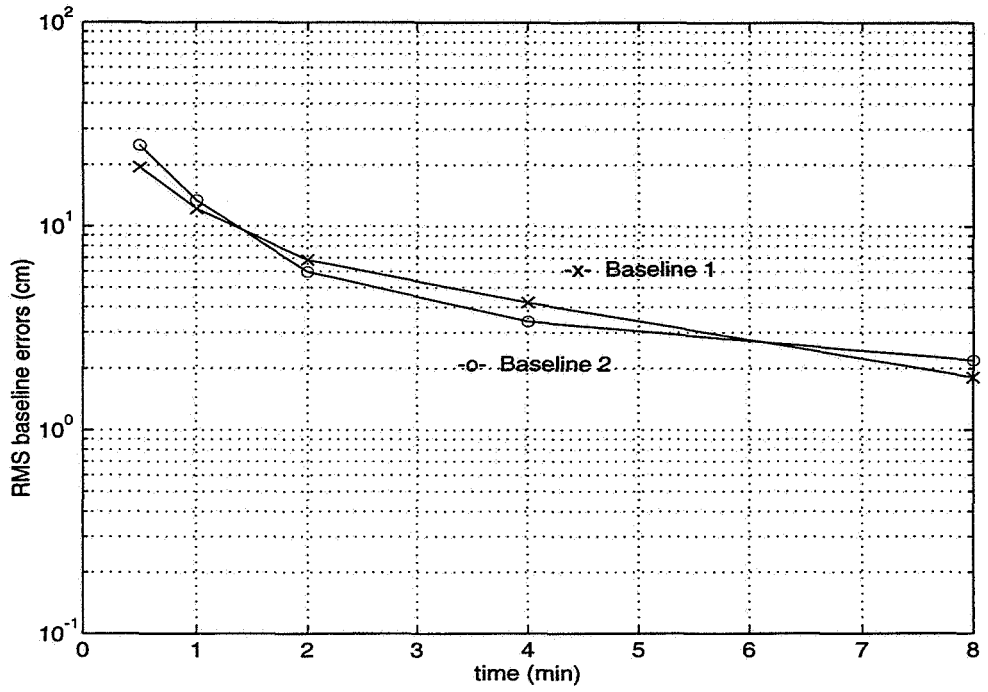

Figure 27: Case 3 RMS Baseline Errors

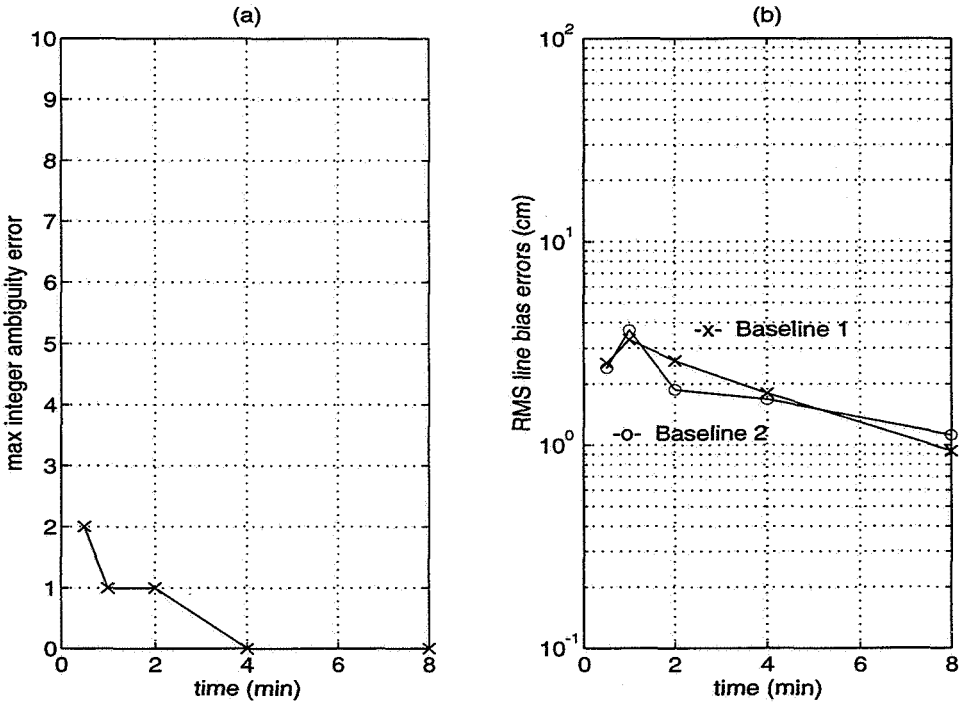

Figure 28: Case 3 Maximum Integer Ambiguity Error and RMS Line Bias Errors

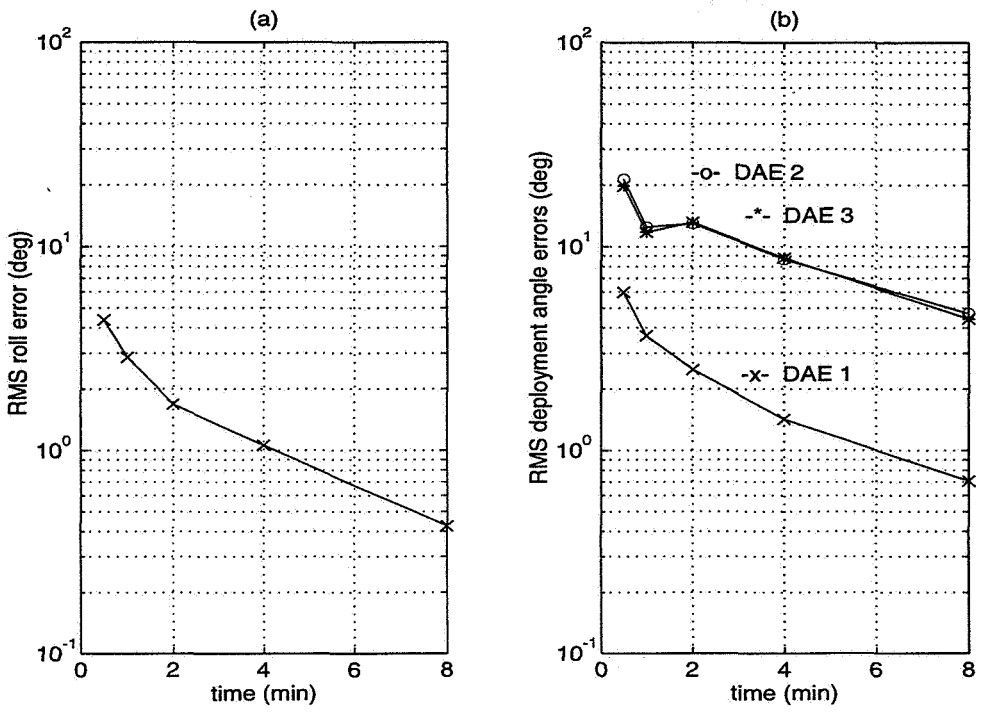

Figure 29: Case 3 RMS Roll Angle and Deployment Angle Errors

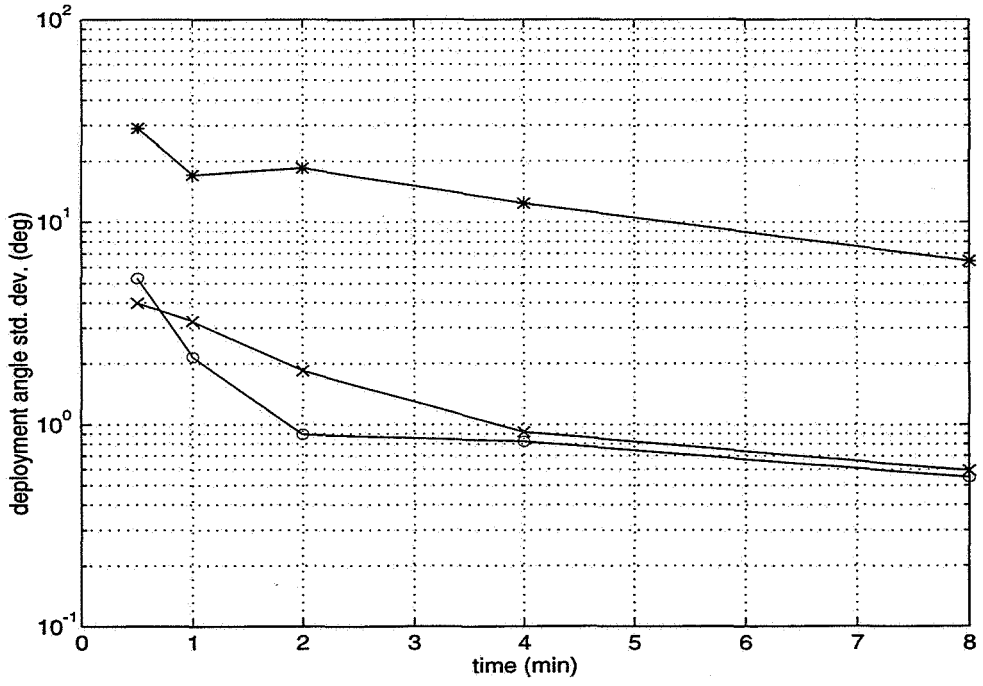

Figure 30: Case 3 Eigenvalues of Deployment Angle Covariance Matrix

The results for the remaining cases are similar to those plotted. In all of the cases, the roll angle is determined within a degree even when the flap angle errors are large. This supports the argument that the roll is independent of flap angles 1 and 3. In each case, the smallest two eigenvalues of the deployment angle covariance are of the same order as the roll angle error. After 8 minutes, these eigenvalues are less than two degrees in all cases and less than 1 degree in most. This is consistent with the RMS baseline errors. An error of 5 cm in a 2.5 m baseline would result in about one degree of error in the roll angle, which would in turn affect the deployment angles by a similar amount.

The previous case studies for the equatorial region have shown that the roll angle may be determined to less than a degree and the deployment angles may be determined to within a degree of their relative positions. For cases 3, 4, and 8, in which one deployment angle is 90°, only 1-2 GPS SV's were visible at the poles for the entire 8 minute period, and so these cases could not be studied. For the remaining cases, four SV's were visible instead of the six available at the equator. However, the results are similar to those for the equator: the roll angles are determined within a degree and the deployment angle errors are correlated to less than a degree.

For all the cases, both at the equator and poles, the integer ambiguities were resolved after 4 minutes. Thus the least-squares solution from 4 minutes worth of data may be sufficient for some purposes. However, 8 minutes of data result in significantly better baseline estimates: the errors are two-thirds to half as great as those resulting from 4 minutes. The comparisons of the RMS baseline errors using 4 and 8 minutes of data for

baseline 1 and 2 are presented in Figure 31 and Figure 32, respectively. Similar comparisons for the polar regions are shown in Figure 33 and Figure 34.

In all cases, both equatorial and polar, using 8 minutes of data gives baselines within at most 4.5 cm of their true values. For such baseline errors, the differences between the deployment angle errors are known with accuracies of 2° or less. However, the fact that one deployment angle error cannot be specifically resolved is unavoidable. The deployment angle errors found here are used in the Kalman filter to be discussed in the following section.

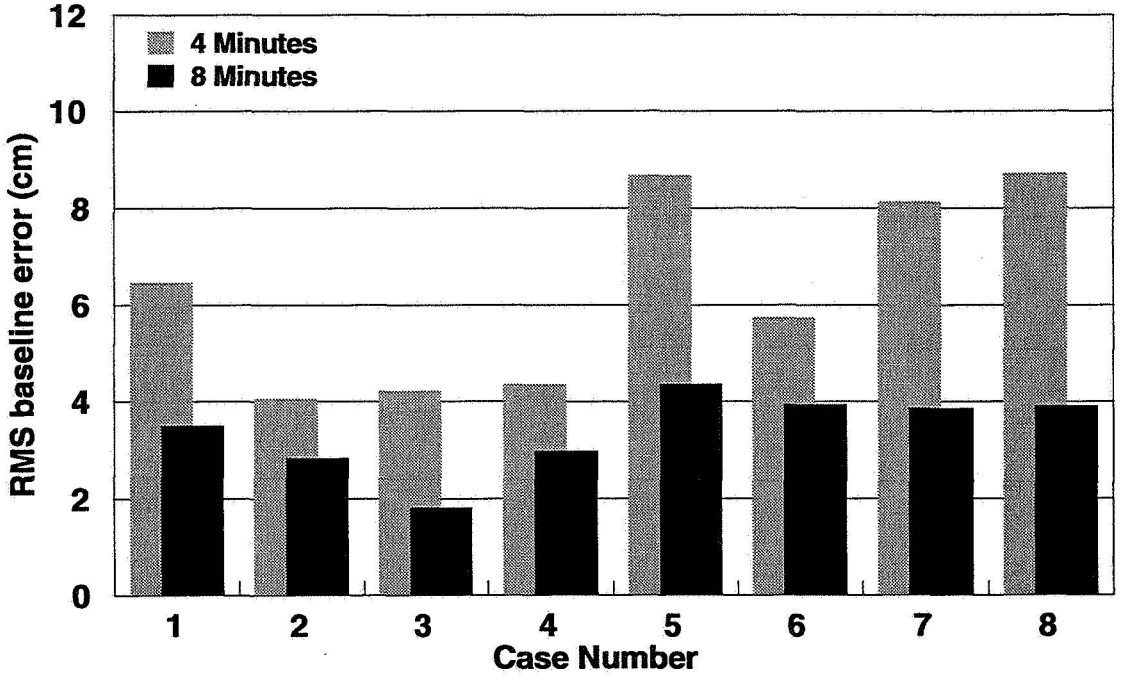

Figure 31: RMS Errors of Baseline 1, Equatorial Cases

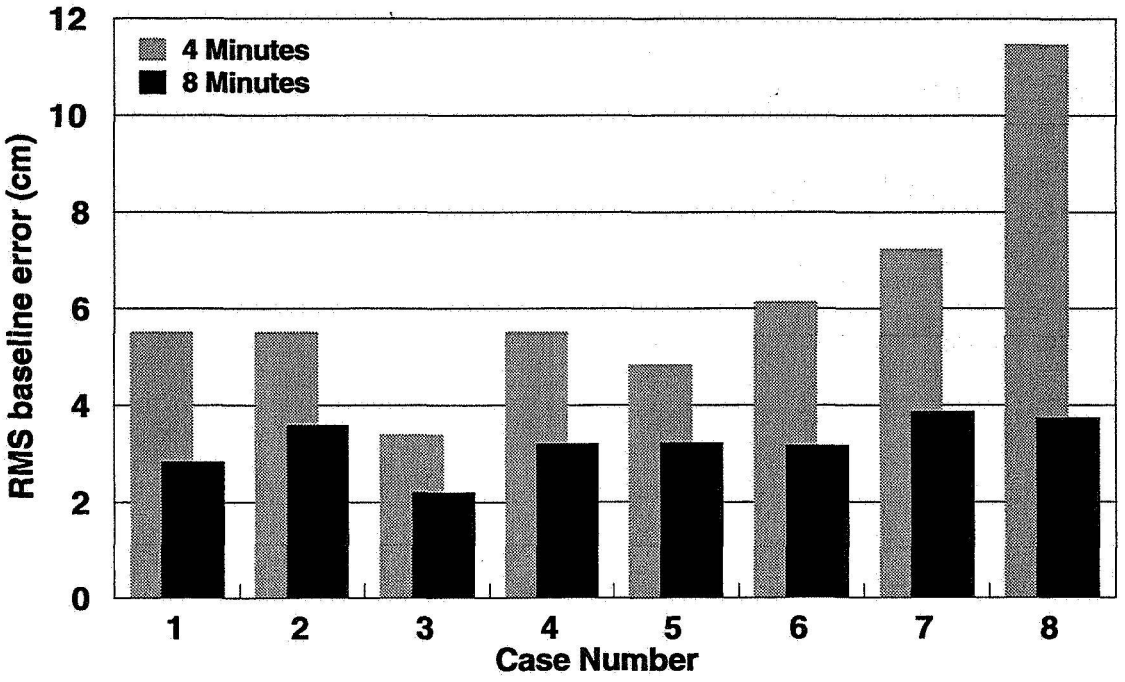

Figure 32: RMS Errors of Baseline 2, Equatorial Cases

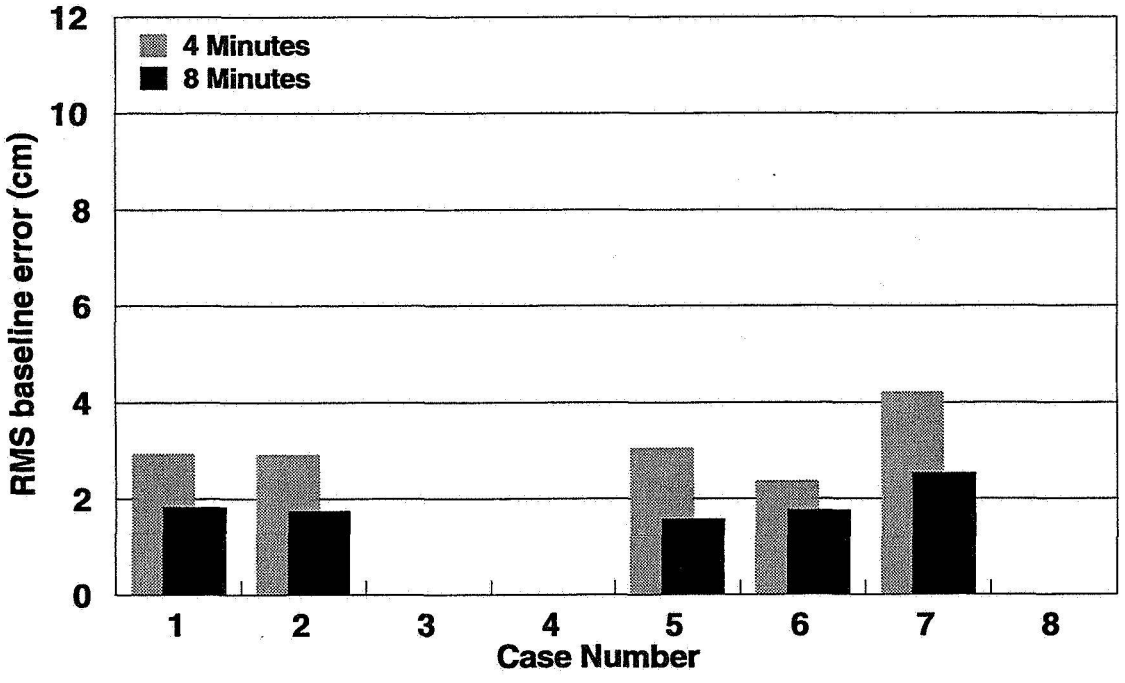

Figure 33: RMS Errors of Baseline 1, Polar Cases

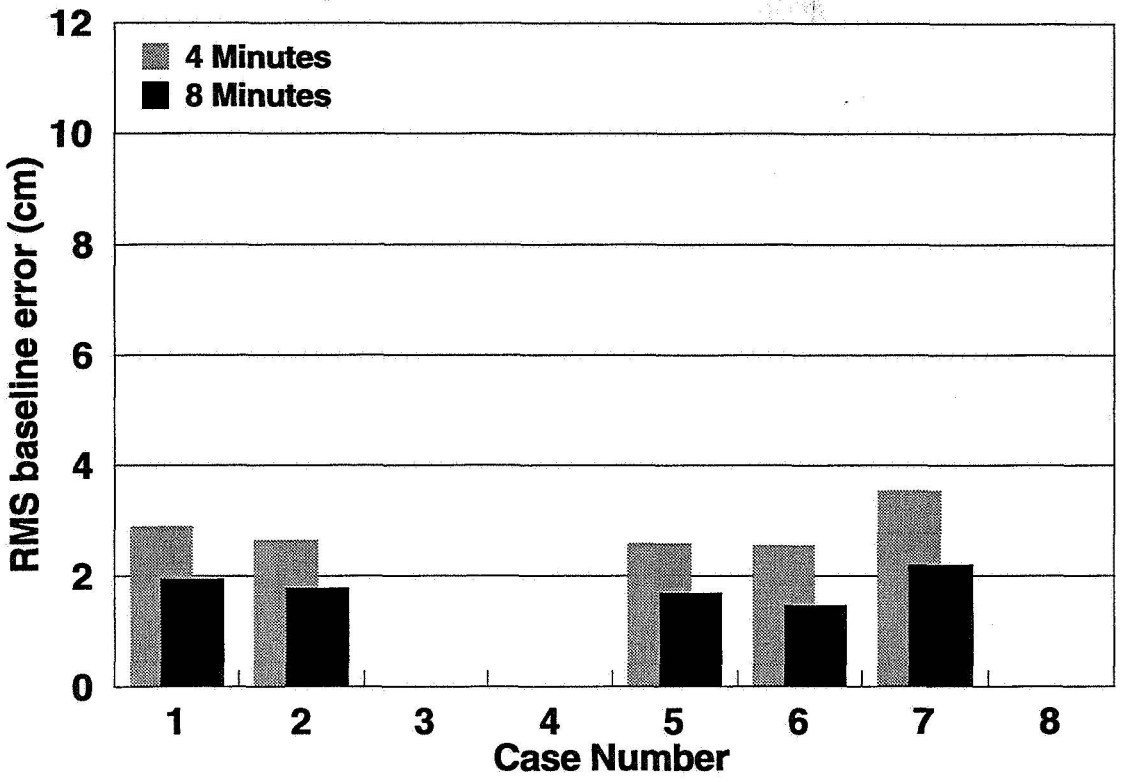

Figure 34: RMS Errors of Baseline 2, Polar Cases

5.2.2 Kalman Filter Attitude Determination

The roll and flap angle estimates resulting from the previous section are now used in a Kalman filter to solve for the attitude of the spacecraft. This is the second stage in the attitude determination process. The formulas of Section 2.2, Kalman Filter Equations, are used to sequentially filter the differential phase measurements created in the simulation. Because they are coupled, the TRACE spacecraft attitude and the flap angles of the solar panels cannot both be determined in a Kalman filter. Some assumptions were necessary to estimate the flap angles in the previous section, but the accuracy depends upon the initial uncertainty in the pitch and yaw angles of TRACE. Thus, the Kalman filter attitude determination is fundamentally limited in its performance capabilities.

After the initialization step of the previous section, the integer ambiguities are resolved for the SV's in sight. This means that the attitude is known within one wavelength, and so the integer ambiguities can be determined for any SV's that subsequently come into view. The determined deployment angle errors are used to form the transformation matrix from the body to solar panel reference frames. Equation 56 is then used to calculate the observed body frame baselines. Lastly, the line biases are as determined from the least-squares solution. The following sections describe the other quantities needed to run the Kalman filter.

5.2.2.1 State Vector and State Transition Matrix

Since the first step of the attitude determination process has provided most of the parameters needed in the differential phase equations, the only parameters to be determined in the Kalman filter are the three Euler angles for the attitude. The three angular rates associated with pitch, roll, and yaw will not be included here. Immediately after step one, then, the estimated attitude is nominal pitch and yaw, and a roll angle as previously computed. The current attitude estimate from the inertial to body frame will be referred to as ${}^{B}\hat{\mathbf{C}}^{I}$. The attitude is formulated as small corrections to the estimate as follows[23]:

$$ {}^{B}\mathbf{C}^{I} = \delta\mathbf{C}^{B}\hat{\mathbf{C}}^{I} = \left(\mathbf{I}+\Theta^{x}\right){}^{B}\hat{\mathbf{C}}^{I} \qquad (65) $$

where $\mathbf{I}$ is the identity matrix and Θ^{x} is the skew-symmetric form of the vector $\delta\theta$:

$$\delta\theta = \begin{bmatrix} \delta\theta_1 \\ \delta\theta_2 \\ \delta\theta_2 \end{bmatrix} \tag{66}$$

Here, $\delta\theta$ is the small correction vector to the attitude and its components form the state vector $\mathbf{x}=[\delta\theta_1\ \delta\theta_2\ \delta\theta_3]^T$ of the filter. Using Equation 66 to define the dynamics of the correction angles, the state transition matrix Φ may be written simply as:

$$\Phi = \mathbf{I} + \Theta^{\times} \tag{67}$$

5.2.2.2 Observation Matrix

To find the observation matrix necessary for the Kalman filter, the derivative of the differential phase with respect to the state elements must be found. The differential phase of Equation 51 written to explicitly include the attitude transformation matrix ${}^{B}\mathbf{C}^{I}$ is

$$\Delta\varphi_{ij} = \frac{\mathbf{b}_i^B \cdot \left({}^{B}\mathbf{C}^{I} \tilde{\mathbf{e}}_j^I \right)}{\lambda} - K_{ij} + \mu_{ij} \tag{68}$$

Using Equation 65 this then becomes

$$\begin{aligned} \Delta\varphi_{ij} &= \frac{\mathbf{b}_i^B \cdot \left\{ \left(\mathbf{I} + \Theta^{\times} \right) {}^{B}\hat{\mathbf{C}}^{I} \tilde{\mathbf{e}}_j^I \right\}}{\lambda} - K_{ij} + \mu_{ij} \\ &= \frac{\left\{ \left(\mathbf{I} + \Theta^{\times} \right) {}^{B}\hat{\mathbf{C}}^{I} \tilde{\mathbf{e}}_j^I \right\}^{\mathrm{T}} \mathbf{b}_i^B}{\lambda} - K_{ij} + \mu_{ij} \\ &= \frac{\left({}^{B}\hat{\mathbf{C}}^{I} \tilde{\mathbf{e}}_j^I \right)^{\mathrm{T}} \left(\mathbf{I} + \Theta^{\times} \right)^{\mathrm{T}} \mathbf{b}_i^B}{\lambda} - K_{ij} + \mu_{ij} \end{aligned} \tag{69}$$

The partial derivative of the differential phase with respect to $\delta\theta$ is thus given by

$$\frac{\partial\left(\Delta\varphi_{ij}\right)}{\partial(\delta\theta)} = \frac{\left({}^{B}\hat{\mathbf{C}}^{I}\tilde{\mathbf{e}}_{j}^{I}\right)^{\mathrm{T}}\mathbf{B}_{i}^{x}}{\lambda} \qquad (70)$$

Here, $\mathbf{B}_i^x$ is the skew-symmetric form of the baseline *i*. Equation 70 produces one 1x3 row of the observation matrix **H** at the time *t*. The two rows of the observation matrix are formed by using Equation 70 for each of the two baselines.

5.2.2.3 State Noise Covariance Matrix

The attitude control system of TRACE is expected to hold sun-lock within 2.5° as a conservative estimate. The limit cycle associated with this maximum pitch and yaw error is taken to be 24 minutes, one-fourth the orbital period of the spacecraft. In one-fourth the limit cycle, then, the pitch and yaw may change by as much as 2.5°. Thus between measurement epochs, the attitude correction angles in the state may change by a maximum of $0.007\Delta t$ degrees, where Δt is the time between measurements in seconds. Thus the state noise covariance is given the value $\mathbf{Q}=(0.007\Delta t)\mathbf{I}$.

5.2.2.4 Measurement Noise Covariance Matrix

The covariance matrix **R** associated with the measurement noise is determined by using data from the JSC experiments described in Chapter 3, Noise Model Development. The covariance matrix of the differential phase residuals for two baselines in that experiment is simply taken as the 2x2 measurement noise covariance matrix for TRACE. The field data was used because of the lower variance of its noise. Note that **R** will not be diagonal because the same antenna is used as the master for each baseline. This introduces correlations into the measurement noise.

5.2.2.5 Kalman Filter Results

With all the parameters defined for the TRACE mission, the Kalman filtering process outlined in Section 2.2 is now implemented. The test attitude history is shown in Figure 35. For demonstration purposes, the pitch and yaw are allowed to vary between ±1.75°, and the roll varies between ±5°., The attitude results for the Kalman filter using perfect knowledge of the deployment angle errors are also included in the figure for reference. The errors are shown in Figure 36; the filter is seen to provide attitude information with 0.2° accuracy.

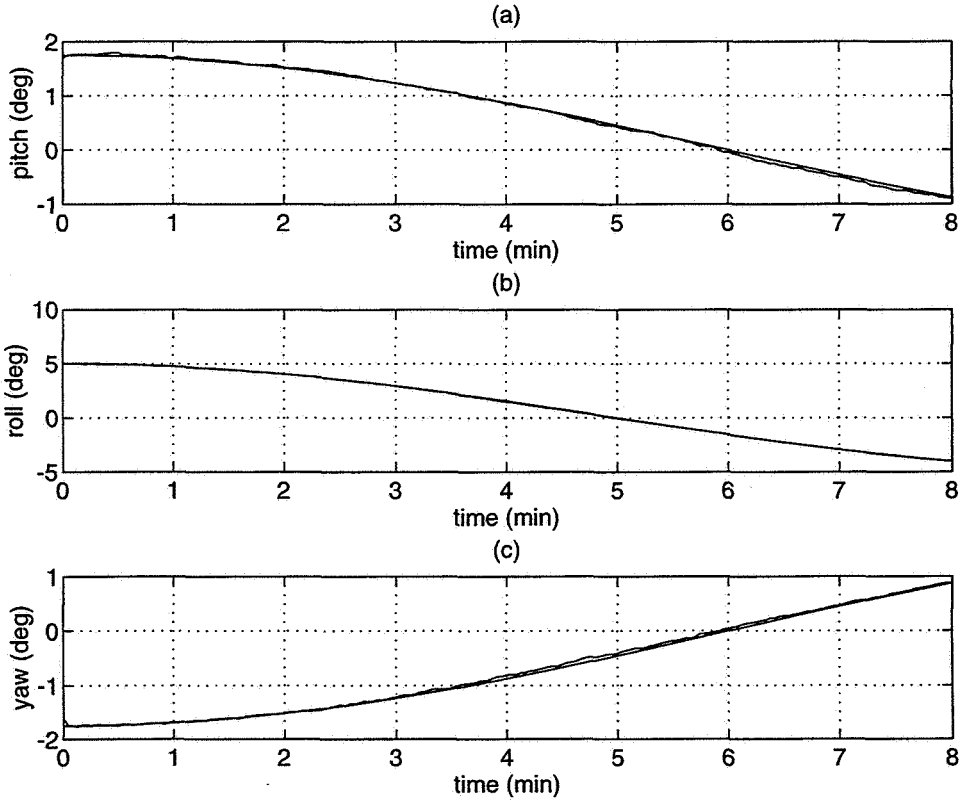

Figure 35: Reference Attitude History

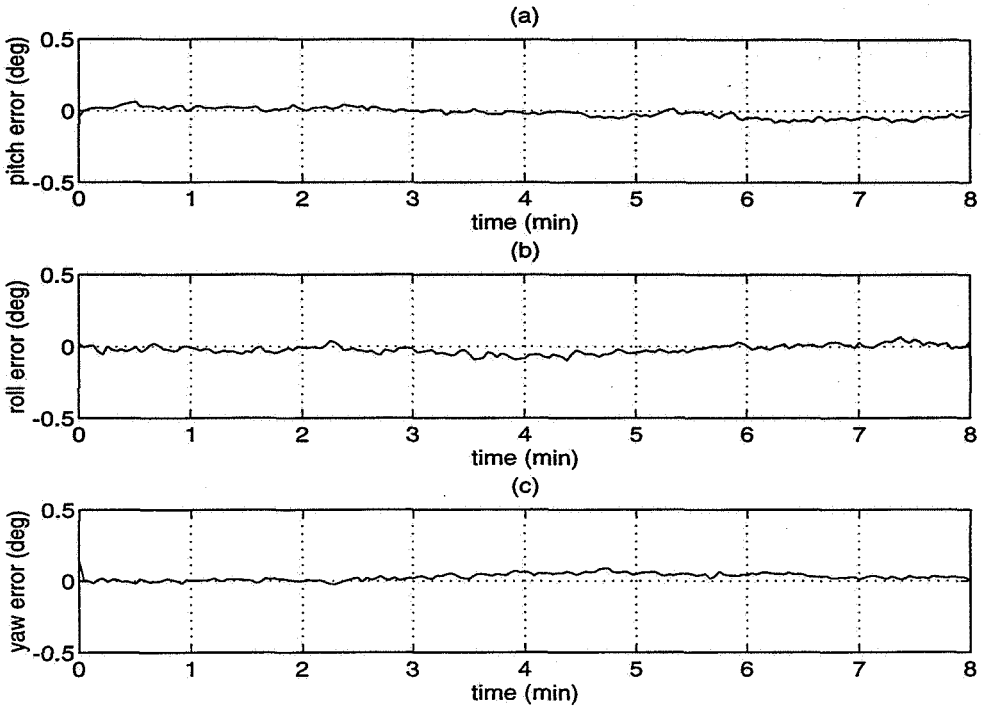

Figure 36: Reference Attitude Errors

The Kalman filter is next run for Case 1, in which the roll angle and all the deployment angles are zero. The results of the initialization step are used to begin the process. The RMS roll angle error was found to be 0.7° after 8 minutes. The final RMS of the deployment angle errors were 12.6°, 12.0°, and 12.2°, respectively (See Figure 24(b)). Both line biases were found within 0.8 cm. Using all these errors in the Kalman filter leads to the attitude history shown in Figure 37. The filter performance seen in Figure 38 is close to that of the perfect assumption comparison case. The offsets seen in all three Euler angles are largely due to the line bias error. The large deployment angle errors, however, had little effect on the attitude accuracy. This is because the plane formed by the three antennas, but not the actual antenna positions, was well-determined.

The results for Case 6 are also presented. In this case, the roll angle is zero and the second and third deployment angle errors are 10°. The RMS errors were found to be 7.5°, 7.0°, and 6.8° for the deployment angles and 0.77° for the roll. The line bias errors had RMS values of 1.3 and 1.1 cm. The attitude history and resulting errors for this case are shown in Figure 39 and Figure 40, respectively. Again, the noticeable offset in the yaw angle is due mainly to the line bias errors. When the simulations for Cases 7 and 8 are run, the resulting attitude errors are consistent with the initial 0.5° uncertainty in the pitch and yaw. This highlights the fundamental limit on the accuracy of the results: deployment angle errors are equivalent to uncertainties in the pitch and yaw and cannot be readily separated.

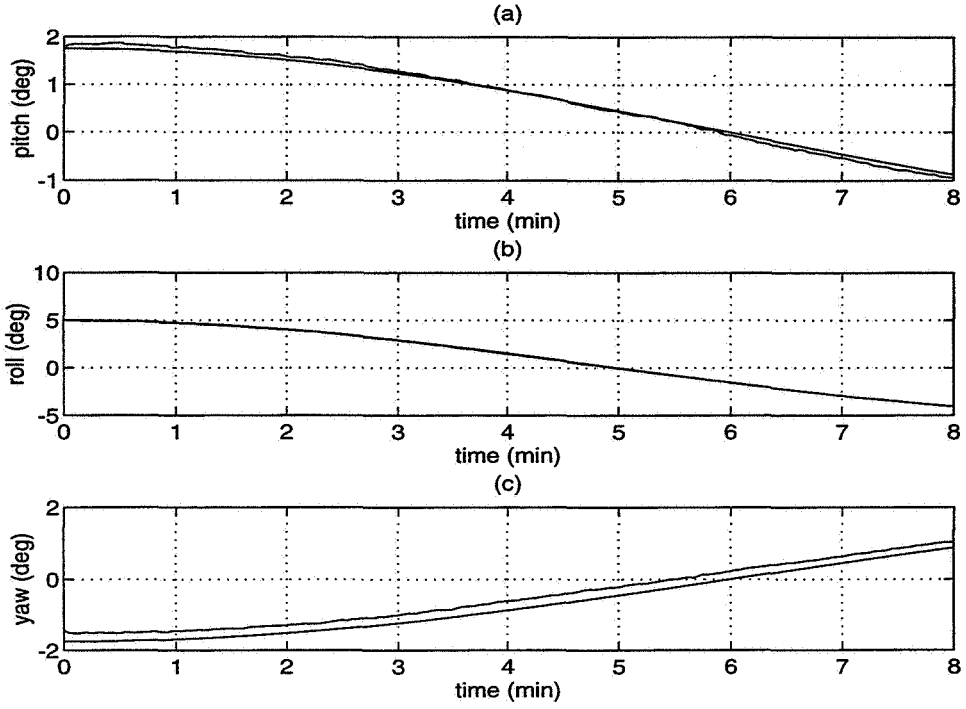

Figure 37: Case 1 Attitude History

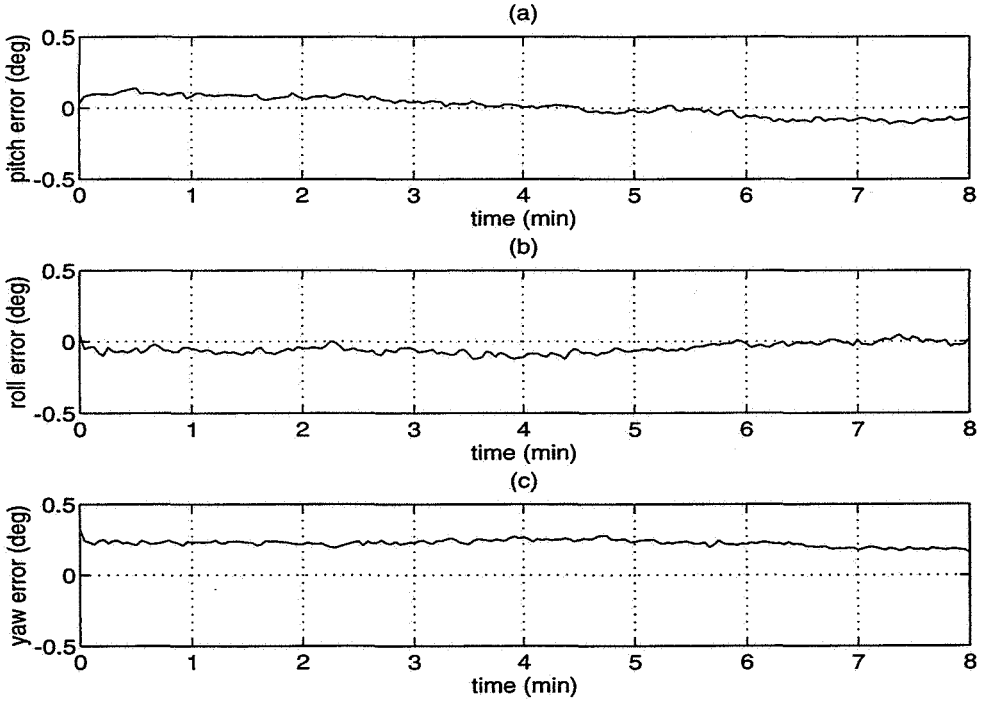

Figure 38: Case 1 Attitude Errors

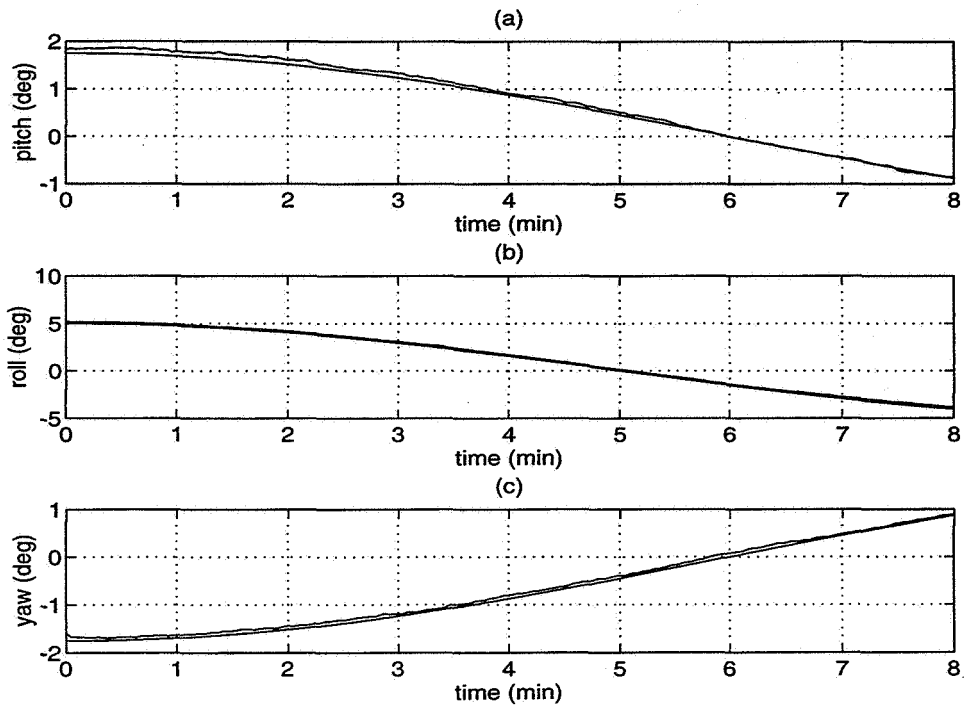

Figure 39: Case 6 Attitude History

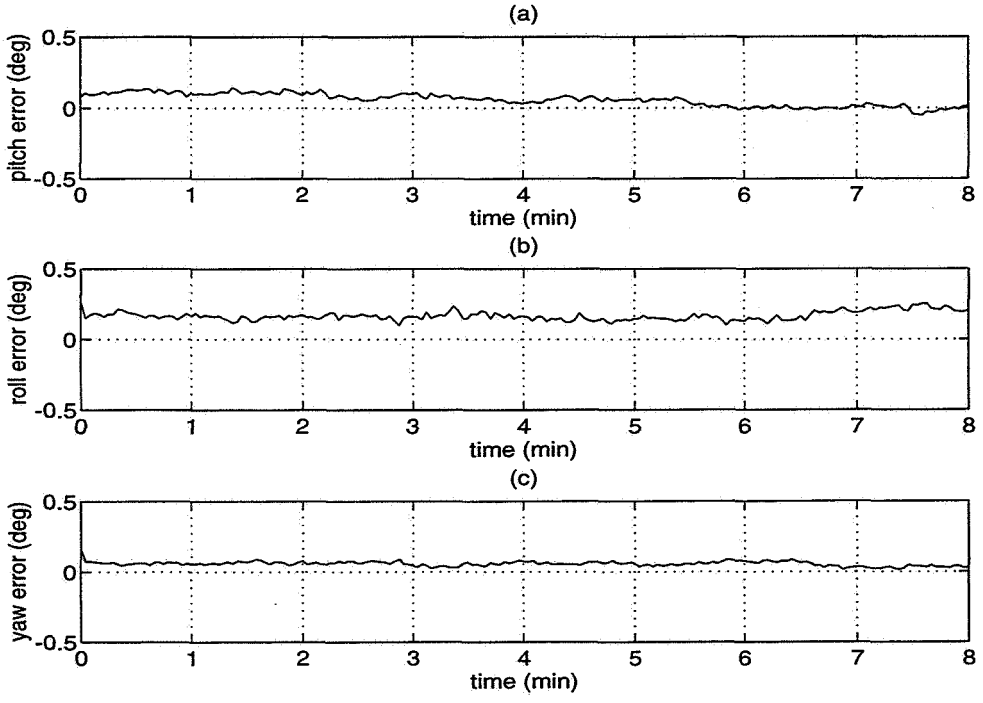

Figure 40: Case 6 Attitude Errors

6. Conclusions and Recommendations

One possible approach to the use of deployable-mounted antennas in GPS attitude determination has been developed in this investigation. Because the baselines may differ greatly from their nominal values, the following two-step procedure for determining attitude is recommended:

1. *Determine baselines using least-squares and assuming nominal attitude.*

    a) *Compare estimates from 2, 4, and 8 minutes of data to ensure convergence at 8 minutes.* Eight minutes of data is recommended because the baseline errors are half those obtained from 4 minutes.

    b) *Use baseline through axis of symmetry to estimate roll angle.* This baseline is projected onto the plane the solar panels would form at full deployment. The angle between the projected vector and the nominal baseline vector is taken as the roll angle. This angle is then used to roll the nominal body frame into the observed body frame.

    c) *Geometrically determine deployment angle errors.* If these errors are all nearly equal but nonzero, it must be decided whether this is a likely scenario. If not, then the errors are probably due to baseline inaccuracies, and the solar panels may be assumed to be fully deployed. Similar arguments may be made for deployment angle errors near 90°.

2. *Use Kalman filter to continuously update attitude using deployment angle errors found in step 1.*

This study has shown that the use of deployables as antenna mounting structures can lead to difficulty in accurately determining attitude in the case of deployment failure. Any initial uncertainty in the pitch and yaw angles for the TRACE spacecraft are indistinguishable from solar panel deployment angle errors. However, for constant pitch and yaw errors within 0.5°, the relative deployment angle errors can be resolved within 1°. These relative errors then lead to final attitude accuracy of 0.5°, even with actual deployment angle errors greater than 10°. This is of course consistent with the original attitude assumption and implies that little or no improvement can be made to the initial pitch and yaw uncertainties. However, the roll angle is insensitive to errors in the deployment angles. In this study, roll could be determined within 0.5° using a 2.5 m baseline through the spacecraft axis of symmetry. Such an accuracy was obtained even for cases in which one of the solar panels affecting the 2.5 m baseline was completely undeployed.

In the simulations, the plane formed by the three antennas could be well-determined, but not the distance of this plane from the origin of the body reference frame. If one of the antennas was known with greater accuracy, say 2 cm, then the positions of the other two could be determined to a similar accuracy. This suggests that at least one antenna should be placed directly on the body of the spacecraft so that its position is known to within a few centimeters. The other antennas could then remain on the solar panels without loss of attitude accuracy.

To further improve the accuracy of the attitude determined by the Kalman filter, the line biases and angular rates of the spacecraft could be included as state elements. The

rates were not included in this study because the sampling period, 2.5 seconds, was short enough that the attitude did not need to be propagated forward in time with rate information. Including the angular rates in the filter may permit longer sampling intervals to be used with little performance degradation, and is recommended for further study.

The determination of the deployment angles errors may be avoided altogether if the baselines, no matter how they are oriented in the nominal body frame, are used to *define* the body frame. However, determining the deployment angle errors of the solar panels allows for a better understanding of the physical condition of the spacecraft. Knowing the positions of the solar panels might allow one to explain, for example, the loss of power from one or more arrays. Additionally, incomplete solar panel deployment could change the moments of inertia of the spacecraft. If the attitude control system was seriously affected, knowledge of the solar panel deployment angle errors could provide the means to correct the problem. Thus the estimation of the deployment angle errors is deemed a worthwhile endeavor.

References

[1] Stein, B. A. and Tsang, W. L., "Stabilization of Low Orbiting Spacecraft Using GPS", *Proceedings of the 47th Annual Meeting of The Institute of Navigation*, Williamsburg, VA, 1991, pp. 5-7.

[2] van Graas, F. and Braasch, M. S., "GPS Interferometric Attitude and Heading Determination: Initial Flight Test Results", *Proceedings of the 47th Annual Meeting of The Institute of Navigation*, Williamsburg, VA, 1991, pp. 183-191.

[3] Lightsey, E. G., Cohen, C. E., and Parkinson, B. W., "Application of GPS Attitude Determination to Gravity Gradient Stabilized Spacecraft", *AIAA Guidance, Navigation, and Control Conference*, Monterey, CA, 1993, p.820.

[4] Hope, A. S., "Ground Test of Satellite Attitude Determination Using GPS", *AAS/AIAA Spaceflight Mechanics Meeting*, Cocoa Beach, FL, 1994.

[5] Axelrad, P. and Ward, L. M., "On-Orbit GPS Based Attitude and Antenna Baseline Estimation", *Proceedings of the ION National Technical Meeting*, San Diego, CA, 1994, pp. 441-450.

[6] Kaplan, M. H., *Modern Spacecraft Dynamics & Control*, Wiley, New York, NY, 1976, pp. 10-13.

[7] Hofmann-Wellenhof, B., Lichtenegger, H. and Collins, J., *Global Positioning System: Theory and Practice*, 2nd Ed., Springer-Verlag Wien, New York, NY, 1992, p. 16.

[8] Van Dierendonck, A. J., Russell, S. S. and Kopitske, E. R., "The GPS Navigation Message", *Navigation: Journal of the Institute of Navigation*, Vol. 25, 1978, pp. 147-165.

[9] Hofmann-Wellenhof, B., Lichtenegger, H. and Collins, J., *Global Positioning System: Theory and Practice*, 2nd Ed., Springer-Verlag Wien, New York, NY, 1992.

[10] van Graas, F. and Braasch, M. S., "GPS Interferometric Attitude and Heading Determination: Initial Flight Test Results", *Proceedings of the 47th Annual Meeting of The Institute of Navigation*, Williamsburg, VA, 1991, pp. 183-191.

[11] Logsdon, T., *The Navstar Global Positioning System*, Van Nostrand Reinhold, New York, NY, 1992, pp. 61-62.

[12] Bozic, S. M., *Digital and Kalman Filtering: An Introduction to Discrete-Time Filtering and Optimum Linear Estimation*, 2nd Ed., Halsted Press, New York, NY, 1994, pp. 120-124.

[13] Hofmann-Wellenhof, B., Lichtenegger, H. and Collins, J., *Global Positioning System: Theory and Practice*, 2nd Ed., Springer-Verlag Wien, New York, NY, 1992, pp. 111-113.

[14]Hope, A. S., "Ground Test of Satellite Attitude Determination Using GPS", *AAS/AIAA Spaceflight Mechanics Meeting*, Cocoa Beach, FL, 1994.

[15]Hardin, J. C., *Introduction to Time Series Analysis*, NASA Reference Publication 1145, 2nd Printing, 1990, pp. 25-28.

[16]Braasch, M. S., "A Signal Model for GPS", *Navigation: Journal of The Institute of Navigation*, Vol. 37, No. 4, 1990-91, pp. 363-377.

[17]Hardin, J. C., *Introduction to Time Series Analysis*, NASA Reference Publication 1145, 2nd Printing, 1990, pp. 130-132.

[18]Ljung, L., *System Identification: Theory for the User*, Prentice-Hall, Englewood Cliffs, NJ, 1987, pp. 69-81.

[19]Ljung, L., *System Identification Toolbox for use with MATLAB: User's Guide*, The MathWorks, Inc., 1988, pp. I.8-I.17.

[20]Hofmann-Wellenhof, B., Lichtenegger, H. and Collins, J., *Global Positioning System: Theory and Practice*, 2nd Ed., Springer-Verlag Wien, New York, NY, 1992, p. 113.

[21]DiPrinzio, M. D. and Tolson, R. H., "Evaluation of GPS Position and Attitude Determination for Automated Rendezvous and Docking Missions", NASA Contractor Report 4614, 1994, pp. 16-18.

[22]Axelrad, P. and Ward, L. M., "On-Orbit GPS Based Attitude & Antenna Baseline Estimation", *Proceedings of the ION National Technical Meeting*, San Diego, CA, 1994, pp. 441-450.

[23]Axelrad, P. and Ward, L. M., "On-Orbit GPS Based Attitude & Antenna Baseline Estimation", *Proceedings of the ION National Technical Meeting*, San Diego, CA, 1994, pp. 441-450.

REPORT DOCUMENTATION PAGE

Form Approved
OMB No. 0704-0188

1. AGENCY USE ONLY *(Leave blank)*	2. REPORT DATE	3. REPORT TYPE AND DATES COVERED
	March 1996	Contractor Report

4. TITLE AND SUBTITLE

GPS Attitude Determination Using Deployable-Mounted Antennas

5. FUNDING NUMBERS

NCC1-104

6. AUTHOR(S)

Michael L. Osborne
Robert H. Tolson

7. PERFORMING ORGANIZATION NAME(S) AND ADDRESS(ES)

The George Washington University
Joint Institute for Advancement of Flight Sciences
NASA Langley Research Center
Hampton, VA 23681-0001

8. PERFORMING ORGANIZATION REPORT NUMBER

9. SPONSORING/MONITORING AGENCY NAME(S) AND ADDRESS(ES)

National Aeronautics and Space Administration
Langley Research Center
Hampton, VA 23681-0001

10. SPONSORING/MONITORING AGENCY REPORT NUMBER

NASA CR-4721

11. SUPPLEMENTARY NOTES

Technical Monitors: L.F.Rowell (LaRC), G. A. Greatorex (GSFC).
The information presented in this report was offered by the first author as a thesis in partial fulfillment of the requirements for the degree of Master of Science, The George Washington University, JIAFS, July 1995.

12a. DISTRIBUTION/AVAILABILITY STATEMENT

Unclassified - Unlimited
Subject Category 18

12b. DISTRIBUTION CODE

13. ABSTRACT *(Maximum 200 words)*

The primary objective of this investigation is to develop a method to solve for spacecraft attitude in the presence of potential incomplete antenna deployment. Most research on the use of the Global Positioning System (GPS) in attitude determination has assumed that the antenna baselines are known to less than 5 centimeters, or one quarter of the GPS signal wavelength. However, if the GPS antennas are mounted on a deployable fixture such as a solar panel, the actual antenna positions will not necessarily be within 5 cm of nominal. Incomplete antenna deployment could cause the baselines to be grossly in error, perhaps by as much as a meter. Overcoming this large uncertainty in order to accurately determine attitude is the focus of this study. To this end, a two-step solution method is proposed. The first step uses a least-squares estimate of the baselines to geometrically calculate the deployment angle errors of the solar panels. For the spacecraft under investigation, the first step determines the baselines to 3-4 cm with 4-8 minutes of data. A Kalman filter is then used to complete the attitude determination process, resulting in typical attitude errors of 0.5°.

14. SUBJECT TERMS	15. NUMBER OF PAGES
Spacecraft attitude, GPS, attitude determination.	94
	16. PRICE CODE: A05

17. SECURITY CLASSIFICATION OF REPORT	18. SECURITY CLASSIFICATION OF THIS PAGE	19. SECURITY CLASSIFICATION OF ABSTRACT	20. LIMITATION OF ABSTRACT
Unclassified	Unclassified	Unclassified	